The Dissertation Committee for Marija Žanić
certifies that this is the approved version of the following dissertation:

Cosmology Driven by Physics Beyond the Standard Model

Committee:

Sonia Paban, Supervisor

Jacques Distler

Daniel Freed

Willy Fischler

Vadim Kaplunovsky

Cosmology Driven by Physics Beyond the Standard Model

by

Marija Žanić, B.S.

DISSERTATION

Presented to the Faculty of the Graduate School of
The University of Texas at Austin
in Partial Fulfillment
of the Requirements
for the Degree of

DOCTOR OF PHILOSOPHY

THE UNIVERSITY OF TEXAS AT AUSTIN
December 2007

to my parents

Acknowledgments

I have had the great honor of being a member of the Weinberg Theory Group over the last several years. Professor Steven Weinberg is such a remarkable scientist and intellectual, and learning cosmology from him was a tremendous privilege. I am very thankful to my advisor, Professor Sonia Paban, who has provided me with years of guidance and advice. I would also like to thank all the other members of the Theory Group: Professors Jacques Distler, Willy Fischler and Vadim Kaplunovsky for sharing their physical insights, especially through their courses on theoretical physics; all the student and postdoc members of the group for numerous useful discussions; Terry Riley for all his help; and Jan Duffy, who made such a difference on so many occasions during my days in the Theory Group. My gratitude goes out to Professor Ernst-Ludwig Florin, for his generous help with preparations for my future career in biological physics, which I am so looking forward to.

I am thankful to dear friends John Reynolds, Michael Frias and Zachary Palmer for their love and support; Alexis Palmer, who has taught me everything I know about being American with so much patience, love and enthusiasm; and Gabrelle Saurage, who has been with me every step of the way on the unimaginably intense and astonishing journey of the first years of motherhood.

I am extremely fortunate to have been brought up by two extraordinary people, Dinka Maretić-Žanić and Gvozdan Žanić, who have given me not only their unconditional love, but also their true respect for me as an individual from as early as I can remember; a gift too rarely given by parents to a child. My late grandmother, Ana Maretić, taught me to be strong and to not sweat the small stuff, and I miss her deeply. I am thankful to my brother-in-law, Žarko Pavlović, for his love and kindness and for always being there for me. I am forever indebted to my loving sister, Ana Žanić Pavlović, who knows me better than I know myself, and whose wisdom, strength and support have been essential to me throughout my life. Finally, I could not imagine my life without my wonderful husband, Radovan Thomas Pavlović, the most generous and selfless person I have ever met, and our son, Andrew, who gives meaning to it all.

Cosmology Driven by Physics Beyond the Standard Model

Publication No. ____________________

Marija Žanić, Ph.D.
The University of Texas at Austin, 2007

Supervisor: Sonia Paban

This dissertation investigates several problems inspired by the interplay of cosmology and theories beyond the Standard Model of particle physics.

The first part of this work is a study of time evolution of unstable $dS_p \times S^q$ configurations with flux in theories of gravity with a cosmological constant. We find that, depending on the flux, these configurations either evolve towards newly identified stable solutions with a smaller final effective cosmological constant, or tend toward decompactification of the internal sphere.

In the second part, we investigate the problem of evolution of vacuum bubbles in inhomogeneous backgrounds. It is expected that the process of inflation will significantly smooth out spatial inhomogeneities. However, the initial conditions for inflation are often taken in the already homogeneous and isotropic FRW form, even though it is assumed that initial homogeneity is not necessary for the onset of inflation. We determine the effects of certain inhomogeneities, introduced in the curvature of the outside spacetime, on the propagation of bubbles, and how these effects differ depending on whether the perspective taken is that of the outside observer or an observer on the bubble.

The last part of the dissertation presents a model for a novel component of the energy density of the universe. The observational limits on the present energy density allow for a component that redshifts like $1/a^2$ and can contribute significantly to the total. We show that one possible origin for such a contribution is that the universe has a toroidal topology with ”wound” scalar fields around its cycles.

Table of Contents

List of Tables

List of Figures

Chapter 1

Introduction

This thesis addresses issues in cosmology inspired by recent developments in high energy physics. Physical phenomena on small scales are remarkably well-described by quantum mechanics, and Einstein's general theory of relativity gives us a clear understanding of the force of gravity, which is usually important only on large, cosmic scales. For a complete physical understanding of the universe, we also need a quantum theory of gravity, which would tell us about how gravity behaves on small scales. Though such a theory is still not fully developed, string theory has emerged as the best current candidate. Over the course of the last decade, cosmological observations have provided us with remarkable data about the universe [1, 2] that can be used to test current theories. Not only does a successful theory have to be consistent with the observed properties of our universe, but also the hope is that current cosmological observations can give us a window into the early universe, and therefore help develop a better understanding of the physics at high energy scales.

Our understanding of the history of the universe comes in the form of the *Big Bang* theory. The Big Bang model employs the general theory of relativity and uses the fact that our universe appears extremely homogeneous and isotropic on very large scales (the so-called *cosmological principle*). The theory predicts that our universe has been expanding from a hot dense plasma to its current state over billions of years. Major support of this model came through the discovery [3] of *Cosmic Microwave Background Radiation* (CMBR), an extremely isotropic radiation with a black-body spectrum. CMBR is comprised of photons remnant from the very early hot universe. These photons stopped scattering off the hot dense plasma once the universe was cold enough for the formation of hydrogen to happen (about 3,000 K), and have been traveling to us ever since and cooling down due to the expansion of the universe.

The Big Bang model is very successful, however, it does not provide for a complete picture of the universe and its evolution. In particular, it assumes the cosmological principle, but does not offer an explanation of why the universe is so homogeneous and isotropic on large scales. Also, on very small scales, the Big Bang model does not address the origin and nature of the observed inhomogeneities of the cosmic microwave background or consequently, the formation of structure in the universe.

The first of these issues, commonly referred to as the *horizon problem*, can be resolved by *inflation*, a period of very rapid accelerated growth at the early stages of the universe [4]. The problem is that the extraordinary isotropy of the universe exists on sizes larger than our present horizon, which is the distance a photon could travel over the age of the universe. Our universe also appears to be very flat, i.e. having nearly zero spatial curvature. Translated to early times of an expanding universe filled with matter and radiation, this means that the universe must have been extremely flat, which seems to be an improbable coincidence and is referred to as the *flatness problem*. The way inflation deals with these problems is that through a period of exponential expansion inflation irons out the inhomogeneities and smoothes out any non-flatness that exists in the small patch of the early universe which corresponds to what we observe today. In addition, inflation resolves another cosmological problem, called the *monopole problem*, by explaining why it is that we do not observe magnetic monopoles, which should be plentiful according to our particle physics theories.

Understanding the observed inhomogeneities in the CMBR requires a physical theory which would explain the density fluctuations in the early universe. In the inflationary theory, such perturbations can arise from vacuum fluctuations of the *inflaton* field, a scalar field which drives the inflation.

Currently there are many models of inflation, each coming with its own set of predictions that can be checked against the observational data. It is expected for a quantum theory of gravity, such as string theory, to provide models of inflation within its framework. Indeed, recent developments in string theory have led to several models of string inflation [5, 6].

Furthermore, string theory needs to be compatible with the present state of the universe. We have strong observational evidence [7] that the universe is currently undergoing accelerated expansion, driven by so-called *dark energy*. The nature of the dark energy is still unknown, and accommodating it in string theory is not an easy task [8].

In recent years one scenario has emerged as a possible way to address both the inflation and the current acceleration of the universe in the realm of string theory. It is a model known as the string theory *landscape* [9]. This controversial model predicts that there exists an enormous number of vacua in string theory (on the order of 10^{500}), some of which will have properties (such as the observed acceleration) of our universe. There have been a lot of efforts put into the concrete realizations of this scenario which, in turn, could lead to a much-desired test of the possible predictions coming from string theory [10].

In addition to the above challenges, string theory requires the existence of extra dimensions, beyond the four spacetime dimensions we are familiar with. The two main proposals for why we do not see the extra dimensions are the *compactification* and the *braneworld* approaches. In the first case, extra dimensions are assumed to be compactified on a tiny scale, so small that we cannot probe them with our current experimental capabilities. The second option is that all matter and forces, except for gravity, are constrained to a four-dimensional subspace (a brane) of the full spacetime.

This thesis addresses several problems related to and inspired by issues described above. In particular, Chapter 2 deals with a toy model which has compactified extra dimensions. The model assumes four-dimensional spacetime in the form of *de Sitter* space, the simplest solution of the Einstein's equations for an accelerating universe. In addition, the model involves several extra dimensions, compactified on a sphere. The extra dimensions are prevented from becoming large by a presence of flux. However, some such constructions are known to be unstable under the perturbations of the spacetime metric [11]. This chapter addresses the time evolution of such spacetimes and finds where it leads.

Chapter 3 investigates the time evolution of the expanding universe in a hypothetical inhomogeneous background. The goal is to provide a better understanding of the constraints on initial conditions for the onset of cosmological inflation. This is particularly important in the context of developing cosmological models within the framework of string theory, where it seems that the background encountered by a growing vacuum bubble would more likely be inhomogeneous.

Chapter 4 explores a model for a novel component of the energy density of the universe (in addition to matter, radiation, and so forth). The model is based on the assumption of toroidal topology of the universe, and it introduces scalar fields that are wound around the torus cycles. This scenario leads to a component which redshifts as $1/a^2$. The observational constraints for the topology and size of the universe as well as present energy density composition are discussed, leading to a bound on the contribution of this component to the present energy density of the universe.

Chapter 5 presents concluding remarks, based on the results obtained in chapters 2-4.

This thesis is mostly based on work presented in [12],[13] and [14].

Chapter 2

Evolution of Gravitationally Unstable de Sitter Compactifications

Compactifications of extra dimensions are a very important subject of study, particularly due to the prediction of string theory which requires the existence of extra dimensions in our own universe. Some simple compactification solutions have been known for decades; in particular Freund and Rubin [15] discovered that spacetimes of dimension $p+q$ naturally compactify to product spaces of the form $dS_p \times S^q$ if an antisymmetric tensor field of dimension $q-1$ is added to the standard Einstein-Hilbert action. It is furthermore interesting to investigate what kind of solutions one obtains if a positive cosmological constant is added to such model.

Bousso, de Wolfe and Myers [11] studied these conditions and were particularly interested in potential entropy bounds that could be established for such compactifications. Namely, it is known that de Sitter space has a finite entropy related to the value of its cosmological constant [16]. Therefore, as argued by Fischler [17] and Banks [18], de Sitter space should be described by a finite-dimensional Hilbert space, containing a total of e^{S_0} independent quantum states. Furthermore, the so-called $\Lambda - N$ correspondence postulates a direct link between the size of the cosmological constant and the dimensionality of the Hilbert space, and one may ask whether specifying the cosmological constant alone is sufficient to determine the size of the corresponding Hilbert space, leading to the so called "N-bound" [19].

In order to address this question, Bousso, de Wolfe and Myers first investigated stability of the above class of $dS_p \times S^q$ solutions under gravitational perturbations. Then they looked into the total entropy of the stable solutions in this class, and found some particular cases where the entropy is unbounded. They therefore found counterexamples of the N-bound and concluded that knowing the cosmological constant does not always lead to a finite observable entropy.

While investigating the gravitational stability of these $dS_p \times S^q$ compactifications, Bousso, de Wolfe and Myers discovered that there are cases in which such compactifications are unstable to gravitational perturbations, and posed a question regarding their future. In this work we address and answer this question by performing numerical simulations of the time evolution of such unstable compactifications.

In what follows, we first present a summary of the solutions described in [19] and then discuss their gravitational stability. Furthermore, we introduce a more general solution of the equations of motion that reduces to the solutions found in [19], and can therefore interpolate between an initial unstable configuration and a final, stable one. We then present the time evolution that results from our numerical analysis.

2.1 Product Spacetimes with Flux

We will consider solutions of the following action:

$$S = \frac{1}{2}\int d^{p+q}x\sqrt{-g}(R - 2\Lambda - \frac{1}{2q!}F_{P_1\ldots P_q}F^{P_1\ldots P_q}), \tag{2.1}$$

in units where M_P in $p+q$ dimensions has been set equal to 1. The cosmological constant Λ will be assumed positive. $F_{P_1\ldots P_q}$ is a totally antisymmetric tensor of rank q. Throughout this chapter we adopt the notation that upper case latin indices run from 1 to $p+q$, greek indices $\mu, \nu, \ldots$ run from 1 to p and greek indices $\alpha, \beta, \ldots$ run from 1 to q. The equations of motion are:

$$G_{MN} = \frac{1}{2(q-1)!}F_{MP_1\ldots P_{q-1}}F_N^{P_1\ldots P_{q-1}} - g_{MN}\;(\Lambda + \frac{1}{4q!}F_{P_1\ldots P_q}F^{P_1\ldots P_q}), \tag{2.2}$$

$$\frac{1}{\sqrt{-g}}\partial_M(\sqrt{-g}F^{MP_1\ldots P_{q-1}}) = 0. \tag{2.3}$$

These equations admit a solution that is a product of two spaces, a Lorentzian and a Riemannian (S^q):

$$ds^2 = -dt^2 + a(t)^2 d^{p-1}\mathbf{x} + R_0^2 d\Omega_q, \tag{2.4}$$

$$R_{\mu\nu} = \frac{p-1}{L^2}g_{\mu\nu}, \tag{2.5}$$

$$R_{\alpha\beta} = \frac{q-1}{R^2}g_{\alpha\beta}, \tag{2.6}$$

with the field strength F_q proportional to the volume form on S^q:

$$F_q = c\,\mathrm{vol}_{S^q}, \qquad \oint \mathrm{vol}_{S^q} = R_0^q\,\Omega_q. \tag{2.7}$$

To be consistent with the notation of [11] we will parametrize the solutions in terms of

$$\mathcal{F} = \frac{c^2}{4\Lambda}. \tag{2.8}$$

Though $\mathcal{F}$ has often in the literature been referred to as the flux, it is clear from (2.7) that the actual flux, with the normalization given above, is also a function of the compactification radius R_0. With a normalization that makes the flux radius independent, $F_q = \frac{c}{R^q(t)}\,\mathrm{vol}_{S^q}$, there are actually two static solutions, instead of one, for some values of c.

The equations of motion for the Lorentzian scale factor, $a(t)$ are:

$$\frac{(p-1)(p-2)}{2}\frac{\dot{a}^2}{a^2} + \frac{(p-1)(p-2)}{2}\frac{k}{a^2} = \Lambda + \Lambda\,\mathcal{F} - \frac{q(q-1)}{2}\frac{1}{R_0^2}, \tag{2.9}$$

where $k = 1, 0, -1$ corresponds to closed, flat or open spaces.

The effective cosmological constant of the p dimensional Lorentzian space , Λ_p, is given by:

$$(p-1)\Lambda_p = \frac{p-1}{L^2} = \frac{2\Lambda}{p+q-2}\left(1-(q-1)\mathcal{F}\right). \tag{2.10}$$

Since Λ has been chosen positive, the effective cosmological constant will be positive as long as

$$0 \leq \mathcal{F} < \frac{1}{q-1}. \tag{2.11}$$

The radius of S^q is given by:

$$\frac{q-1}{R_0^2} = \frac{2\Lambda}{p+q-2}\left(1+(p-1)\mathcal{F}\right). \tag{2.12}$$

2.2 Stability under Gravitational Perturbations

In this section we will summarize the results of [20] and [11] to show the existence of unstable radion modes (i.e. modes that correspond to the perturbation of the size of the sphere S^q), whose evolution we will study in the following sections.

2.2.1 Linearized Fluctuations and Gauge Fixing

Linearized fluctuations of the metric are defined by:

$$\begin{aligned}
\delta g_{\mu\nu} &= h_{\mu\nu} = H_{\mu\nu} - \frac{1}{p-2} g_{\mu\nu} h^{\alpha}_{\alpha}, && (2.13)\\
\delta g_{\mu\alpha} &= h_{\mu\alpha}, && (2.14)\\
\delta g_{\alpha\beta} &= h_{\alpha\beta}, && (2.15)
\end{aligned}$$

where (2.13) reflects the linearized Weyl shift.

$H_{\mu\nu}$ and $h_{\alpha\beta}$ can be decomposed into trace and traceless parts:

$$\begin{aligned}
H_{\mu\nu} &= H_{(\mu\nu)} + \frac{1}{p} g_{\mu\nu} H^{\rho}_{\rho}, && (2.16)\\
h_{\alpha\beta} &= h_{(\alpha\beta)} + \frac{1}{q} g_{\alpha\beta} h^{\gamma}_{\gamma}, && (2.17)
\end{aligned}$$

where $g^{\mu\nu} H_{(\mu\nu)} = g^{\alpha\beta} h_{(\alpha\beta)} = 0$.

Gauge fixing is obtained by imposing de Donder gauge conditions:

$$\nabla^{\alpha} h_{(\alpha\beta)} = \nabla^{\alpha} h_{\alpha\mu} = 0. \qquad (2.18)$$

Linearized fluctuations of the form field are defined by:

$$\begin{aligned} \delta A_{q-1} &= a_{q-1}, \qquad (2.19)\\ \delta F_q &\equiv f_q = da_{q-1}, \qquad (2.20) \end{aligned}$$

where $F_q = dA_{q-1}$.

Since A_{q-1} contains gauge degrees of freedom, analogous to the electromagnetic gauge potential, we further impose Lorentz-type gauge conditions:

$$\nabla^\alpha a_{\alpha\beta_2\ldots\beta_{q-1}} = \nabla^\alpha a_{\alpha\beta_2\ldots\beta_{q-2}\mu} = \ldots = \nabla^\alpha a_{\alpha\mu_2\ldots\mu_{q-1}} = 0. \tag{2.21}$$

The fluctuations can be expanded in spherical harmonics:

$$\begin{aligned} H_{(\mu\nu)}(x,y) &= \sum_I H^I_{(\mu\nu)}(x)Y^I(y), \qquad (2.22)\\ H^\mu_\mu(x,y) &= \sum_I H^I(x)Y^I(y), \qquad (2.23)\\ h_{(\alpha\beta)}(x,y) &= \sum_I \Phi^I(x)Y^I_{(\alpha\beta)}(y), \qquad (2.24)\\ h^\alpha_\alpha(x,y) &= \sum_I \pi^I(x)Y^I(y), \qquad (2.25)\\ h_{\mu\alpha}(x,y) &= \sum_I B^I_\mu(x)Y^I_{(\alpha}(y), \qquad (2.26)\\ a_{\beta_1\ldots\beta_{q-1}} &= \sum_I b^I(x)\epsilon^\alpha{}_{\beta_1\ldots\beta_{q-1}}\nabla_\alpha Y^I(y), \qquad (2.27)\\ a_{\mu\beta_2\ldots\beta_{q-1}} &= \sum_I b^I_\mu(x)\epsilon^{\alpha\beta}{}_{\beta_2\ldots\beta_{q-1}}\nabla_{[\alpha}Y^I_{\beta]}(y), \qquad (2.28)\\ &\vdots\\ a_{\mu_1\ldots\mu_{q-1}} &= \sum_I b^I_{\mu_1\ldots\mu_{q-1}}(x)Y^I(y), \qquad (2.29) \end{aligned}$$

where I is an index over the possible spherical harmonics of the corresponding tensor representation.

Any n-form on a compact q-dimensional manifold without boundary can be represented as a sum of an exact, a co-exact and a harmonic n-form. Lorentz conditions (2.21) require the exact contribution to vanish, and since our manifold is a sphere, there are no nontrivial harmonic forms, and therefore our gauge potentials (2.28) are expanded as co-exact forms, i.e. curls.

For further simplification we also define:

$$b(x,y) \equiv \sum_I b^I(x) Y^I(y), \tag{2.30}$$

$$b_{\mu\alpha}(x,y) \equiv \sum_I b^I_\mu(x) Y^I_\alpha(y). \tag{2.31}$$

2.2.2 Linearized Einstein and Form Field Equations

Linearized perturbations of the Ricci tensor are given by:

$$\begin{aligned} \delta R_{MN} = &-\frac{1}{2}(\Box_x + \Box_y) h_{MN} + \nabla_M \nabla_N h^P_P - \nabla_M \nabla^P h_{PN} - \nabla_N \nabla^P h_{PM} \\ &- 2R_{MPQN} h^{PQ} - R^P_M h_{NP} - R^p_N h_{MP}, \end{aligned} \tag{2.32}$$

where $\Box_x \equiv g^{\mu\nu}\nabla_\mu\nabla_\nu$, and $\Box_y \equiv g^{\alpha\beta}\nabla_\alpha\nabla_\beta$.

In components, this corresponds to:

$$\begin{aligned}\delta R_{\mu\nu} =& -\frac{1}{2}[(\Box_x + \Box_y)(H_{\mu\nu} - \frac{1}{p-2}g_{\mu\nu}h^{\gamma}_{\gamma}) + \nabla_\mu\nabla_\nu(H^{\rho}_{\rho} - \frac{2}{p-2}h^{\gamma}_{\gamma}) \\ & - \nabla_\mu\nabla^\rho(H_{\rho\nu} - \frac{1}{p-2}g_{\rho\nu}h^{\gamma}_{\gamma}) - \nabla_\nu\nabla^\rho(H_{\rho\mu} - \frac{1}{p-2}g_{\rho\mu}h^{\gamma}_{\gamma}) \\ & - 2R_{\mu\rho\sigma\nu}(H^{\rho\sigma} - \frac{1}{p-2}g^{\rho\sigma}h^{\gamma}_{\gamma}) - R^{\rho}_{\mu}(H_{\rho\nu} - \frac{1}{p-2}g_{\rho\nu}h^{\gamma}_{\gamma}) \\ & - R^{\rho}_{\nu}(H_{\rho\mu} - \frac{1}{p-2}g_{\rho\mu}h^{\gamma}_{\gamma})],\end{aligned} \tag{2.33}$$

$$\begin{aligned}\delta R_{\mu\alpha} =& -\frac{1}{2}[\Box_x h_{\mu\alpha} - \nabla_\mu\nabla^\nu h_{\nu\alpha} - R^{\nu}_{\mu}h_{\nu\alpha} + \Box_y h_{\mu\alpha} - R^{\beta}_{\alpha}h_{\beta\mu} - \nabla^{\nu}_{\alpha}h_{\nu\mu} \\ & + \nabla_\mu\nabla_\alpha(H^{\rho}_{\rho} - \frac{2}{p-2}h^{\gamma}_{\gamma}) - \nabla_\mu\nabla^\beta h_{\beta\alpha}],\end{aligned} \tag{2.34}$$

$$\begin{aligned}\delta R_{\alpha\beta} =& -\frac{1}{2}[(\Box_x + \Box_y)h_{(\alpha\beta)} - 2R_{\alpha\gamma\delta\beta}h^{(\gamma\delta)} - R^{\gamma}_{\alpha}h_{(\gamma\beta)} - R^{\gamma}_{\beta}h_{(\gamma\alpha)} \\ & + \frac{1}{q}g_{\alpha\beta}(\Box_x + \Box_y)h^{\gamma}_{\gamma} - \left(\frac{2}{q} + \frac{2}{p-2}\right)\nabla_\alpha\nabla_\beta h^{\gamma}_{\gamma} + \nabla_\alpha\nabla_\beta H^{\mu}_{\mu} \\ & - \nabla_\alpha\nabla^\mu h_{\mu\beta} - \nabla_\beta\nabla^\mu h_{\mu\alpha}].\end{aligned} \tag{2.35}$$

We will be using Ricci form of Einstein's equations, $R_{MN} = S_{MN}$, where $S_{MN} \equiv T_{MN} + \frac{1}{2-D}g_{MN}T^{P}_{P}$.

Corresponding components on the right hand side of the Einstein's equations are given by:

$$\begin{aligned}\delta S_{\mu\nu} =& \frac{c^2(q-1)}{2(D-2)}h_{\mu\nu} + \frac{q(q-1)c^2}{2(D-2)q!}g_{\mu\nu}h^{\alpha\beta}\epsilon_{\alpha\gamma_2\ldots\gamma_q}\epsilon_{\beta}^{\gamma_2\ldots\gamma_q} \\ & - \frac{c(q-1)}{D-2}g_{\mu\nu}(f\cdot\epsilon) + \frac{2\Lambda}{D-2}h_{\mu\nu},\end{aligned} \tag{2.36}$$

$$\delta S_{\mu\alpha} = \frac{c}{2}\nabla_\mu\nabla_\alpha b + \frac{c}{2}(\Box_y b_{\mu\alpha} - R^{\beta}_{\alpha}b_{\mu\beta}) - \frac{c^2(q-1)}{2(D-2)}h_{\mu\alpha}, \tag{2.37}$$

$$\delta S_{\alpha\beta} = \frac{p-1}{D-2} g_{\alpha\beta} \Box_y cb + \frac{q-1}{R^2} h_{(\alpha\beta)} - \frac{(q-1)^2}{qR^2} g_{\alpha\beta} h^{\gamma}_{\gamma}, \tag{2.38}$$

where $f \cdot \epsilon \equiv f_{\alpha_1 \ldots \alpha_q} \epsilon^{\alpha_1 \ldots \alpha_q}/q!$.

We also expand the equation of motion for the form field (2.3) to linear order in perturbations and obtain:

$$\begin{aligned} \nabla^M f_{M\beta_2 \ldots \beta_q} - c g^{\mu\nu} \delta\Gamma^{\gamma}_{\mu\nu} \epsilon_{\gamma\beta_2 \ldots \beta_q} - c g^{\gamma\delta} \delta\Gamma^{\theta}_{\gamma\delta} \epsilon_{\theta\beta_2 \ldots \beta_q} \\ - c(q-1) g^{\gamma\delta} \delta\Gamma^{\theta}_{\gamma\beta_2} \epsilon_{\delta\theta\beta_3 \ldots \beta_q} = 0, \end{aligned} \tag{2.39}$$

$$\nabla^M f_{M\mu\beta_3 \ldots \beta_q} - c g^{\gamma\alpha} \delta\Gamma^{\delta}_{\gamma\mu} \epsilon_{\alpha\delta\beta_3 \ldots \beta_q} = 0. \tag{2.40}$$

2.2.3 Scalar Perturbations

Using the expansion into spherical harmonics, (2.22) - (2.29), we can obtain equations of motions for particular modes of perturbation. In what follows we will only be interested in the scalar perturbations, and will therefore concentrate on the corresponding equations.

From (2.33) and (2.36) we obtain:

$$\begin{aligned} \Bigg[\left(\Box_x + \Box_y - \frac{2(q-1)^2}{R_0^2} + \frac{4\Lambda(p-2)}{D-2} \right) \pi^I + \Box_y \left(H^I - \frac{2(D-2)}{q(p-2)} \pi^I \right) \\ + \frac{2q(p-1)}{D-2} \Box_y c b^I \Bigg] Y^I = 0. \end{aligned} \tag{2.41}$$

Equations (2.35) and (2.38) yield:

$$\left(H^I - \frac{2(D-2)}{q(p-2)} \pi^I \right) \nabla_{(\alpha} \nabla_{\beta)} Y^I = 0. \tag{2.42}$$

Finally, from (2.39):

$$\nabla_\alpha \left((\Box_x + \Box_y) b^I + \frac{c}{2} H^I - \frac{c(p-1)}{p-2} \pi^I \right) Y^I = 0. \tag{2.43}$$

Let us first consider the case where no derivatives of spherical harmonics Y^I vanish. Equation (2.42) allows us to eliminate H^I in favor of π^I:

$$H^I = -\frac{2(D-2)}{q(p-2)} \pi^I, \tag{2.44}$$

which can be substituted into (2.43):

$$\left((\Box_x + \Box_y) b^I + \frac{c(q-1)}{q} \pi^I \right) Y^I = 0. \tag{2.45}$$

Combining (2.41) with (2.45) gives the coupled system of equations:

$$L^2 \Box_x \begin{pmatrix} cb^I \\ \pi^I \end{pmatrix} = \begin{pmatrix} \bar{\lambda}^I & \frac{2}{q}(\alpha + (p-1)(D-2)) \\ \frac{2q(p-1)}{D-2} \bar{\lambda}^I & \bar{\lambda}^I + \frac{2(p-2)}{(D-2)} \alpha + 2(p-1)^2 \end{pmatrix} \begin{pmatrix} cb^I \\ \pi^I \end{pmatrix}, \tag{2.46}$$

where $\alpha \equiv 2\Lambda L^2 = 2\frac{\Lambda}{\Lambda_p}$, and $\bar{\lambda}^I$ is the rescaled eigenvalue of the compact Laplacian:

$$-L^2 \Box_y Y^I \equiv \bar{\lambda}^I Y^I = \left(\frac{L^2}{R_0^2} \right) \lambda^I Y^I, \tag{2.47}$$

and for S^q λ takes values $k(k+q-1)$, $k \in \mathbf{Z}_+$.

After diagonalization we obtain the mass spectrum for this coupled system:

$$m_\pm^2(\bar{\lambda}) L^2 = \bar{\lambda} + A \pm \sqrt{A^2 + 4B\bar{\lambda}}, \tag{2.48}$$

where

$$A = \frac{p-2}{D-2} \alpha - (p-1)^2 = \frac{(p-1)^2(q-1)}{1-(q-1)\mathcal{F}} (\mathcal{F} - \mathcal{F}_s), \tag{2.49}$$

$$B = \frac{p-1}{D-2}\alpha - (p-1)^2 = \frac{(p-1)^2(q-1)}{1-(q-1)\mathfrak{F}}\mathfrak{F}, \tag{2.50}$$

$$\mathfrak{F}_s \equiv \frac{1}{(p-1)(q-1)}. \tag{2.51}$$

Since the dS_p solutions exist in the range $0 \leq \mathfrak{F} \leq \mathfrak{F}_m = \frac{1}{q-1}$, B is always positive, and A changes sign at $\mathfrak{F} = \mathfrak{F}_s$.

To identify unstable modes, we need to look for tachyonic modes. The minimum mass is obtained for:

$$\bar{\lambda}_{min} = \frac{4B^2 - A^2}{4B}, \tag{2.52}$$

for which:

$$m_+^2(\bar{\lambda}_{min})L^2 = \bar{\lambda}_{min} + A + 2B. \tag{2.53}$$

This is always positive, since $\bar{\lambda}_{min} > 0$ and $B > 0$ imply $A + 2B > 0$ and $2B - A > 0$. On the lower branch:

$$m_-^2(\bar{\lambda}_{min})L^2 = \bar{\lambda}_{min} - (2B - A) = -\frac{(2B-A)^2}{4B}, \tag{2.54}$$

which will lead to some tachyonic modes.

In particular, $\bar{\lambda}$ for which $m_-^2 L^2$ is negative must be in the range:

$$0 < \bar{\lambda} < \bar{\lambda}_0 \equiv 4B - 2A = \frac{2(p-1)^2(q-1)}{1-(q-1)\mathfrak{F}}(\mathfrak{F} + \mathfrak{F}_s). \tag{2.55}$$

We see that if any modes with $k \geq 3$ are tachyonic, $k = 2$ mode has to be tachyonic as well. We are therefore interested in finding out when is the inequality (2.55) satisfied if $k = 2$. We obtain that this is the case only for $q \geq 4$ and

$$\mathcal{F} > \mathcal{F}_t \equiv \frac{2}{q(q-3)(p-1)}. \tag{2.56}$$

For $k = 1$, $\nabla_{(\alpha}\nabla_{\beta)}Y^I = 0$, and therefore (2.44) can not be used. In that case we use equation (2.43) to eliminate H^I in favor of π^I and b^I. Substituting into (2.41) and using that $\Box_y = -\frac{q}{R^2}$ for a sphere S^q, gives:

$$\left(\Box_x - \frac{q(2q-1)}{R_0^2}\right)\left(\pi^I + \frac{q(p-1)}{(q-1)(D-2)}cb^I\right) + \frac{4\Lambda(p-2)}{D-2}\pi^I = 0, \tag{2.57}$$

which has the same mass as would be obtained from the upper branch of (2.48) for $k = 1$, and is therefore positive.

Finally, for $k = 0$, all derivatives of Y^I vanish, and the only nontrivial equation is (2.41), which reduces to:

$$\left(\Box_x - \frac{2(q-1)^2}{R_0^2} + \frac{4\Lambda(p-2)}{D-2}\right)\pi^I = 0. \tag{2.58}$$

In this case the mass is given by:

$$m_0^2 L^2 = 2A. \tag{2.59}$$

Note that this is on the upper branch only for $\mathcal{F} > \mathcal{F}_s$. However, for $\mathcal{F} < \mathcal{F}_s$ this mode is tachyonic.

Taking all modes into account, $dS_p \times S^q$ solutions will be stable only for:

$$\mathcal{F}_s \leq \mathcal{F} \leq \mathcal{F}_t. \tag{2.60}$$

For $q = 2$ and $q = 3$ only $k = 0$ mode is unstable, and therefore compact S^2 and S^3 are unstable for $\mathcal{F} \leq \mathcal{F}_t$ only.

For $q = 4$, (2.60) implies stability in the range of flux $1/[3(p-1)] \leq \mathcal{F} \leq 1/[2(p-1)]$.

For $q \geq 5$ it turns out that $\mathcal{F}_t < \mathcal{F}_s$, and therefore instabilities occur at all values of $\mathcal{F}$.

The following table summarizes the regions of stability as a function of the free dimensionless parameter $\mathcal{F}$ and the dimension of the Riemannian space q as derived in [11].

Table 2.1: $dS_p \times S^q$ Regions of Stability.

	$dS_p \times S^q$		Minkowski $\times S^q$
q	*unstable*	*stable*	
2	$0 \leq \mathcal{F} < \frac{1}{(p-1)}$	$\frac{1}{(p-1)} \leq \mathcal{F} < 1$	$\mathcal{F} = 1$
3	$0 \leq \mathcal{F} < \frac{1}{2(p-1)}$	$\frac{1}{2(p-1)} \leq \mathcal{F} < \frac{1}{2}$	$\mathcal{F} = \frac{1}{2}$
4	$0 \leq \mathcal{F} < \frac{1}{3(p-1)}, \frac{1}{2(p-1)} < \mathcal{F} < \frac{1}{3}$	$\frac{1}{3(p-1)} \leq \mathcal{F} < \frac{1}{2(p-1)}$	$\mathcal{F} = \frac{1}{3}$
≥ 5	$0 \leq \mathcal{F} < \frac{1}{q-1}$	–	$\mathcal{F} = \frac{1}{q-1}$

Not reflected in the previous table is the fact that the number of unstable modes increases as a function of q. For $q = 2,$ and $q = 3$ there is only one unstable mode. It corresponds to the radius of S^q. For $q \geq 4$ other modes became tachyonic as well.

2.3 Evolution of Unstable Spacetimes

There is a broader set of solutions to (2.2) and (2.3) that do not correspond to a product spacetime. They are of the form:

$$ds^2 = -dt^2 + a(t)^2 d^{p-1}\mathbf{x} + R(t)^2 d\Omega_q, \tag{2.61}$$

$$F_q = \frac{f}{R^q(t)}\,\mathrm{vol}_{S^q} \qquad \oint \mathrm{vol}_{S^q} = R(t)^q\,\Omega_q. \tag{2.62}$$

In this case, the normalization of the differential form F_q is fixed by the equations of motion.

The corresponding equations of motion are:

$$\frac{q(q-1)}{2R^2}(1+\dot{R}^2) + \frac{(p-1)(p-2)}{2}\frac{\dot{a}^2}{a^2} + q(p-1)\frac{\dot{R}\,\dot{a}}{R\,a} = \Lambda\left(1+\frac{\beta}{\Lambda^q R^{2q}}\right), \tag{2.63}$$

$$\begin{aligned}\frac{q(q-1)}{2R^2}(1+\dot{R}^2) + \frac{(p-2)(p-3)}{2}\frac{\dot{a}^2}{a^2} + q(p-2)\frac{\dot{R}\,\dot{a}}{R\,a}+ \\ +(p-2)\frac{\ddot{a}}{a} + q\frac{\ddot{R}}{R} = \Lambda\left(1+\frac{\beta}{\Lambda^q R^{2q}}\right),\end{aligned} \tag{2.64}$$

$$\begin{aligned}\frac{(q-2)(q-1)}{2R^2}(1+\dot{R}^2) + \frac{(p-1)(p-2)}{2}\frac{\dot{a}^2}{a^2} + (q-1)(p-1)\frac{\dot{R}\,\dot{a}}{R\,a}+ \\ +(p-1)\frac{\ddot{a}}{a} + (q-1)\frac{\ddot{R}}{R} = \Lambda\left(1-\frac{\beta}{\Lambda^q R^{2q}}\right),\end{aligned} \tag{2.65}$$

where $\frac{\beta}{\Lambda^q} = \frac{f^2}{4\Lambda}$. To lighten these already complicated equations we have made the assumption that $k=0$, the generalization to $k=\pm 1$ is straightforward.

These equations can be reduced into an equation for the breathing mode of the sphere, often called the radion, $R(t)$:

$$\begin{aligned}\ddot{R} = &\frac{q+p-2}{p-2}\frac{\dot{R}^2}{R}\\ &\mp \frac{p-1}{p-2}\dot{R}\sqrt{\frac{q(p+q-2)}{p-1}\frac{\dot{R}^2}{R^2} - 2\frac{p-2}{p-1}\left[\frac{q(q-1)}{2R^2} - \Lambda\left(1+\frac{\beta}{\Lambda^q R^{2q}}\right)\right]} - \frac{dV(R)}{dR},\end{aligned} \tag{2.66}$$

where the potential

$$V(R) = -\frac{\Lambda R^2}{p+q-2} + \frac{(p-1)}{(q-1)(p+q-2)}\frac{1}{(\Lambda R^2)^{q-1}} + (q-1)\ln(R). \tag{2.67}$$

The evolution of $a(t)$ is given by:

$$\begin{aligned}\frac{\dot{a}}{a} = &-\frac{q}{p-2}\frac{\dot{R}}{R}\\ &\pm \frac{1}{p-2}\sqrt{\frac{q(p+q-2)}{p-1}\frac{\dot{R}^2}{R^2} - 2\frac{p-2}{p-1}\left[\frac{q(q-1)}{2R^2} - \Lambda(1+\frac{\beta/\Lambda^q}{R^{2q}})\right]}.\end{aligned} \tag{2.68}$$

The initial conditions, i.e. the sign of $\frac{\dot{a}}{a}$ at $\dot{R} = 0$, and R equal the radius of the unstable point, decide which branch of the equations (2.66), (2.68) to consider.

As long as the flux is nonvanishing and relatively small; $0 < \beta_s$, where

$$\beta_s = \frac{(q-1)^{2q-1}}{p-1}\left(\frac{p+q-2}{2q}\right)^q, \tag{2.69}$$

the radion potential will always have two stationary solutions, one stable and one unstable. There is a solution to the equations of motion that corresponds to the field $R(t)$ sitting on the maximum. In this case, the geometry factorizes

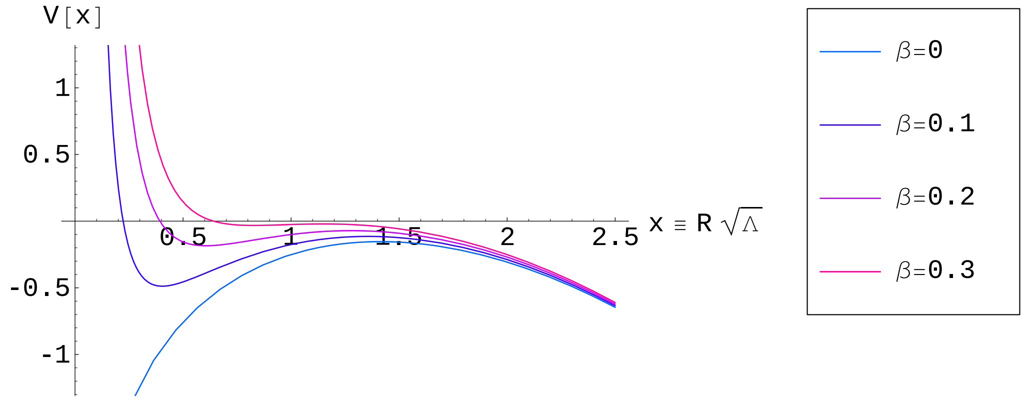

Figure 2.1: Potential for the field $R(t)$ as a function of the flux, β, when $p = 4$ and $q = 2$.

and corresponds to a $dS_p \times S_q$ space. There are also solutions that correspond to $R(t)$ sitting in the minimum. In these cases, the corresponding geometry also factorizes into the product of the spaces $L_p \times S_q$. The Lorentzian signature space will be a (A)dS or flat Minkowski depending on the value of β. In particular, for $\beta_m < \beta < \beta_s$, where

$$\beta_m = \frac{(q-1)^{2q-1}}{2^q}, \tag{2.70}$$

the Lorentzian signature space will also be a de Sitter space.

We are interested in studying the evolution of the unstable solutions away from the maximum. The equations (2.66), (2.68) will capture such an evolution provided that $R(t)$ is the only mode excited along the path away from the maximum. The analysis of [11] proves that this is indeed the only excited mode around the extrema of the potential, provided that $q = 2, 3$, for

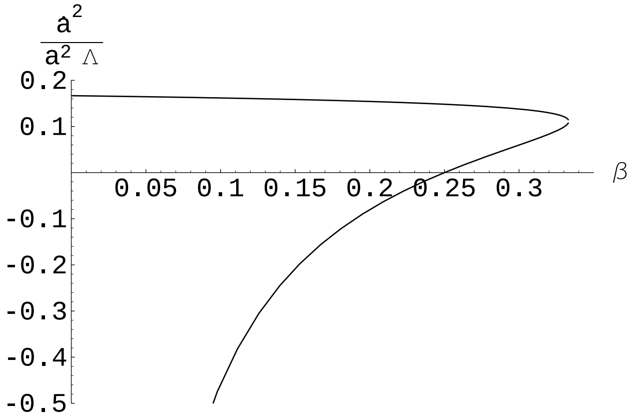

Figure 2.2: Value of $\frac{\dot{a}^2}{a^2}$ at the stationary points as a function of the initial condition β. The upper branch corresponds to the unstable point and the lower branch corresponds to the stable point. (Case $p = 4$, $q = 2$.)

$q \geq 4$ there will be other unstable modes. In this work we will restrict our attention to the first two cases, and leave the analysis of $q \geq 4$ to future work.

2.4 Results

In this section we report on the numerical solution of the equations (2.66), (2.68). An example of the code used in Mathematica for these numerical simulations can be found in Appendix.

It is useful to distinguish between two cases:

- When the minimum of the potential corresponds to another de Sitter solution ($\beta_m < \beta < \beta_s$)
- When the minimum of the potential corresponds to an Anti de Sitter solution ($0 < \beta < \beta_m$)

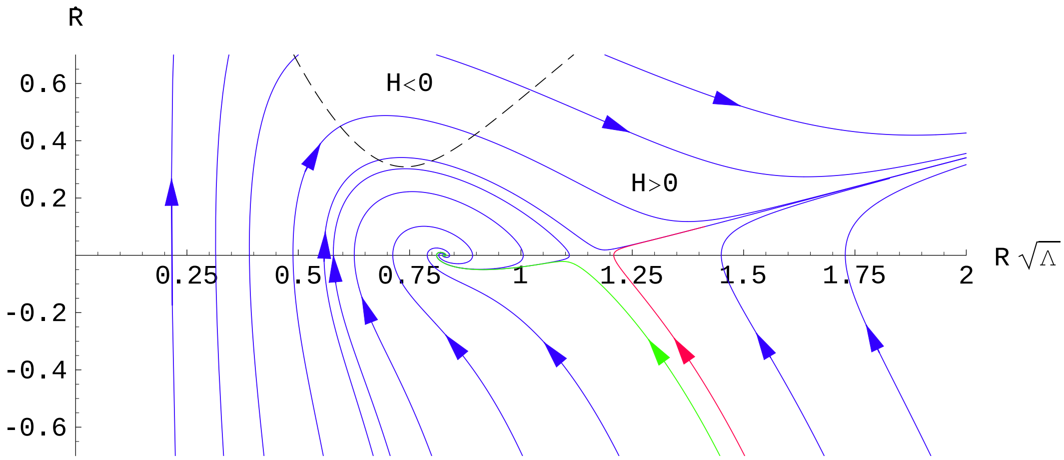

Figure 2.3: Numerical evolution for $p = 4$, $q = 2$, $\beta = 0.3$. The arrows indicate the direction of time evolution.

2.4.1 $\beta_m < \beta < \beta_s$

Let us choose the initial condition such that $\dot{a}/a > 0$, namely, we start with an expanding de Sitter space. The numerical analysis shows that the evolution from the unstable $dS_p \times S^q$ in this case leads either to a decompactification of the compact dimensions, or to another, stable $dS_p \times S^q$ solution, see Figure 2.3.

In the case of decompactification, the expansion rate of the radius of the sphere S^q asymptotes to:

$$\frac{\dot{R}}{R} = \sqrt{\frac{2\Lambda}{(D-1)(D-2)}}, \tag{2.71}$$

where $D = p + q$.

It is interesting to note that this expansion rate matches the asymptotic effective Hubble constant for the de Sitter space, i.e. $\dot{R}/R = \dot{a}/a \text{as } R, a \to \infty$.

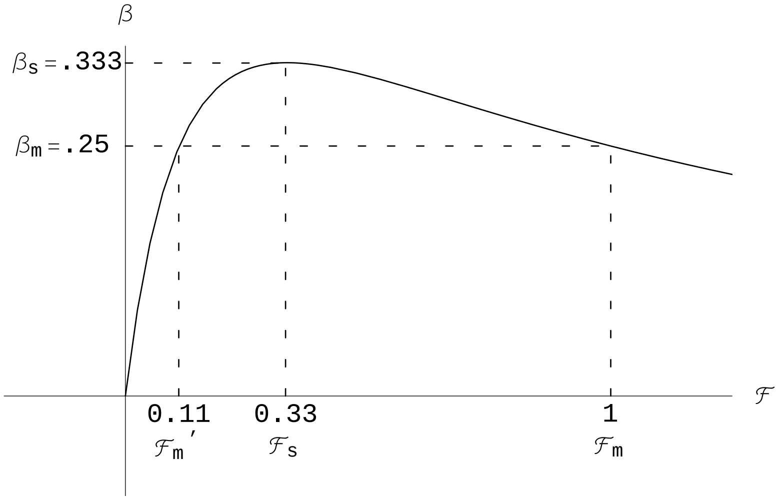

Figure 2.4: Flux β as a function of parameter $\mathfrak{F}$, when $p = 4$ and $q = 2$.

This agrees with the result found in [21], because this fast evolution erases all the information about the initial flux.

The other direction of evolution from the unstable $dS_p \times S^q$, with these initial conditions, leads to a stable $dS_p \times S^q$ solution. The two solutions are characterized by the same value of β. Namely, for a static solution we have:

$$\beta/\Lambda^q = \mathfrak{F}R^{2q}, \tag{2.72}$$

$$R^2 = \frac{(q-1)(D-2)}{2\Lambda[1+(p-1)\mathfrak{F}]}. \tag{2.73}$$

For a particular value of β we have two static solutions related by:

$$\frac{\mathfrak{F}_f}{\mathfrak{F}_i} = \left(\frac{1+(p-1)\mathfrak{F}_f}{1+(p-1)\mathfrak{F}_i}\right)^q. \tag{2.74}$$

The stable solution will always have a smaller radius R than the initial, unstable one. The two are related by:

$$R_f^2 = \frac{1+(p-1)\mathfrak{F}_i}{1+(p-1)\mathfrak{F}_f} R_i^2. \tag{2.75}$$

The effective cosmological constant for the de Sitter is given by (2.10), and it therefore changes:

$$\left(\frac{\dot{a}}{a}\right)_f^2 = \frac{1+(1-q)\mathfrak{F}_f}{1+(1-q)\mathfrak{F}_i} \left(\frac{\dot{a}}{a}\right)_i^2. \tag{2.76}$$

In particular, for $p = 4$ and $q = 2$ we have:

$$\mathfrak{F}_f = \frac{1}{9\mathfrak{F}_i}, \tag{2.77}$$

$$R_f^2 = \frac{2}{\Lambda} - R_i^2 = 3\mathfrak{F}_i R_i^2, \tag{2.78}$$

$$\left(\frac{\dot{a}}{a}\right)_f^2 = \frac{(9\mathfrak{F}_i - 1)}{9\mathfrak{F}_i(1-\mathfrak{F}_i)} \left(\frac{\dot{a}}{a}\right)_i^2, \tag{2.79}$$

$$\Lambda_{4f} = \frac{\Lambda_{4i} - \frac{4}{27}\Lambda}{6\Lambda_{4i} - \Lambda}\Lambda. \tag{2.80}$$

Notice that the final effective cosmological constant can be made very small compared with the initial. The radius of the internal sphere will, however, remain within the same order of magnitude of the initial one.

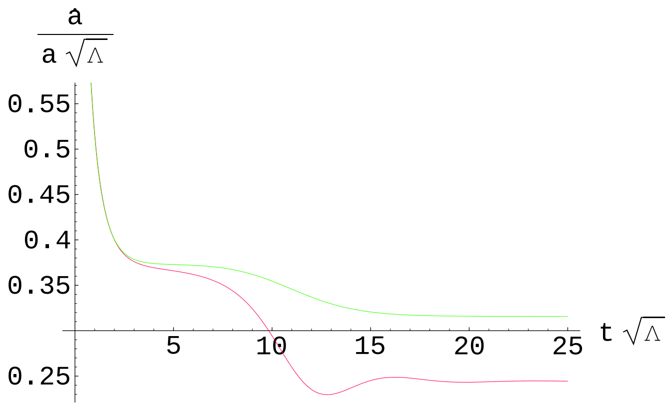

Figure 2.5: The evolution of effective Hubble rate for $p = 4$, $q = 2$. (The colors match the numerical evolution in Figure 2.3)

Let us compare the entropies of the initial and the final solution:

$$\begin{aligned} \frac{S(dS_4 \times S^2)_f}{S(dS_4 \times S^2)_i} &= \frac{A(dS_4)_f \times V(S^2)_f}{A(dS_4)_i \times V(S^2)_i} \\ &= \frac{(1-\mathcal{F}_i)(1+3\mathcal{F}_i)}{(1-\mathcal{F}_i)(1+3\mathcal{F}_i)} \\ &= 27(\mathcal{F}_i)^2 \frac{1-\mathcal{F}_i}{9\mathcal{F}_i - 1} > 1, \end{aligned} \tag{2.81}$$

as long as, $\frac{1}{9} < \mathcal{F}_i < \frac{1}{3}$, which corresponds to our initial unstable static solution.

Now let's look at the situation where the initial conditions are chosen such that the de Sitter component of the space is initially contracting, $\dot{a}/a < 0$ (See Figure 2.6). In this case, the numerical evolution shows that the internal dimensions necessarily decompactify, while the initial de Sitter dimensions keep contracting. This result may appear surprising, at first, when the initial velocity at the unstable point is taken to be negative, i.e. $\dot{R} < 0$. These initial conditions choose the negative branch in (2.68) and hence the positive branch

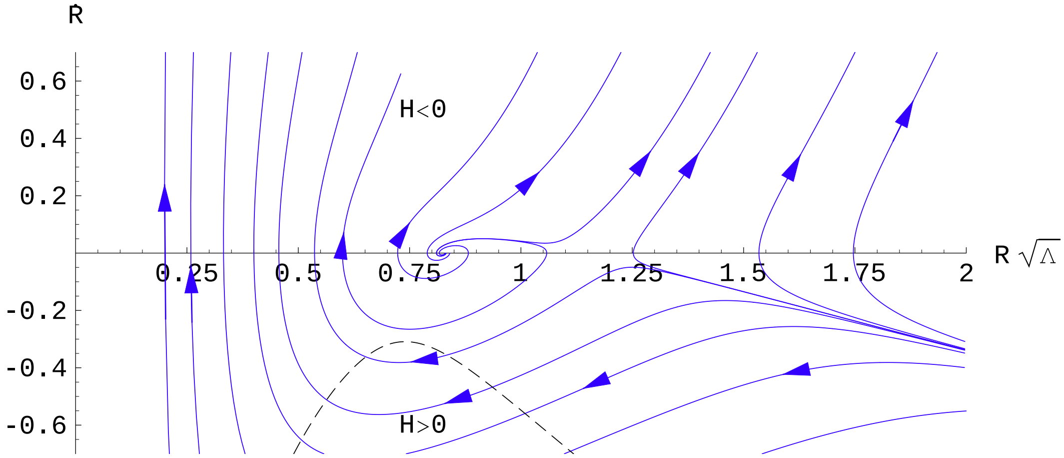

Figure 2.6: Numerical evolution for $p = 4$, $q = 2$, $\beta = 0.3$

in (2.66). The friction force in (2.66) is then big enough to overcome the force generated by the potential.

The crunching solution should (2.61) asymptotically become a Kasner type solution. We did not use this ansatz in the numerical analysis that led to Figure 2.6.

2.4.2 $0 < \beta < \beta_m$

When the flux β is very small, only one of the static solutions corresponds to a de Sitter compactification, the other solution corresponds to an anti de Sitter space. In this case the numerical solution in both branches (either initially contracting (Figure 2.7), or expanding (Figure 2.8) de Sitter phase) leads to a decompactification of the inner space, while the initially de Sitter components either expand or contract, depending on the initial condi-

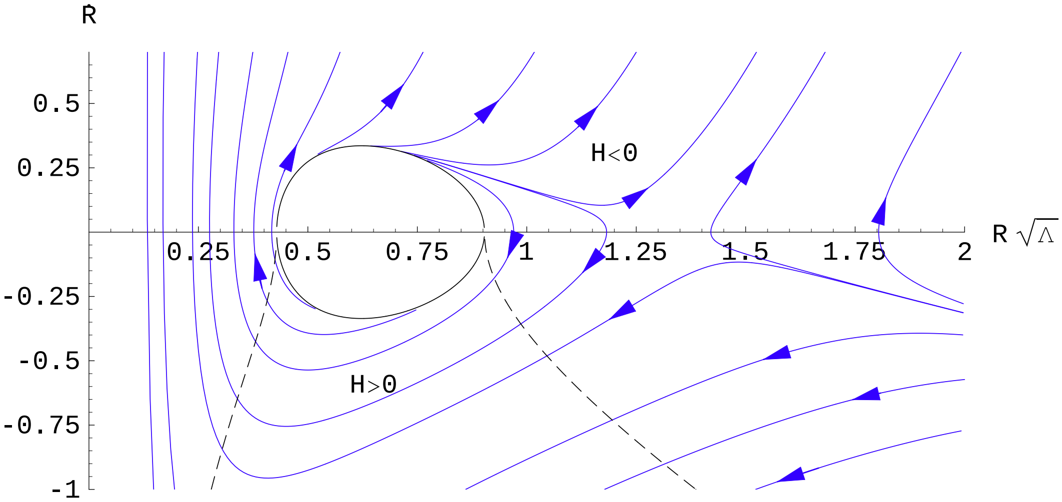

Figure 2.7: Numerical evolution for $p = 4$, $q = 2$,$\beta = 0.15$ or equivalently Anti de Sitter minimum.

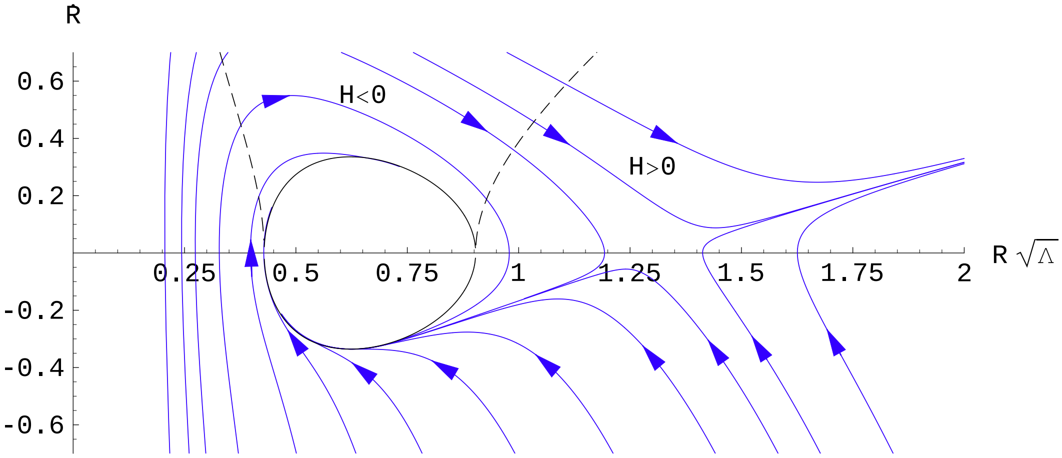

Figure 2.8: Numerical evolution for $p = 4$, $q = 2$, $\beta = 0.15$ or equivalently Anti de Sitter minimum.

tions and the initial direction of the numerical evolution. This is a sensible result. The classical trajectories studied here cannot connect spaces with different spacial curvatures. Given the ansatz for the metric (2.61) the initial de Sitter configuration can be either flat or closed while the final anti de Sitter configuration has to be open.

2.5 Conclusions

In this chapter we have studied the evolution of gravitationally unstable $dS_p \times S^q$ compactifications. We have identified an additional static stable solution that only exists for a certain interval of fluxes. Under certain conditions the evolution leads to this static solution. The other possible final states correspond to a decompactifying internal sphere, while the de Sitter space may either expand or contract.

This work answers the question about the fate of these solutions, originally posed in [19]. A similar analysis, in the absence of flux, was recently done by Contaldi, Kofman and Peloso [21]. It is unclear to what extent the lessons learned here translate into more realistic models, e.g. [22, 23]. In fact, Giddings and Myers [24] have studied these types of models and argued that positive vacuum energy, together with extra dimensions renders the four-dimensional spacetime unstable toward decompactification of the extra dimensions. Our study is purely classical and does not incorporate the effect of thermal fluctuations or tunneling considered in [24].

After this work was completed, we learned that the time evolution of these configurations had already been studied in the past [25, 26]. The goal of these earlier papers was to use the unstable mode as the inflaton mode. Our results present a more complete analysis of all the initial conditions and agree with them when these conditions overlap.

Chapter 3

Bubble Propagation in Gravitationally Inhomogeneous Backgrounds

Although propagation of bubbles in homogeneous cosmological backgrounds has been amply studied [27]-[29], bubble propagation in inhomogeneous backgrounds is virtually unexplored [30]. Since tunneling is of great importance [31, 32] in populating the string landscape [9, 22], the evolution of a new universe through an old one is a problem that needs a better understanding.

One reason for the lack of emphasis on inhomogeneous backgrounds is the cosmic no-hair conjecture [16, 33], which states that the evolution of an expanding universe with a cosmological constant will eventually become dominated by the cosmological constant and asymptote to a de Sitter space. In particular, the cosmic no-hair conjecture implies that inhomogeneous backgrounds containing a cosmological constant (like the ones constructed on Landscape vacua) will evolve toward 'ironing out' such inhomogeneities, and therefore it would make sense to confine the studies of bubble propagation to homogeneous backgrounds. To the best of our knowledge, the cosmic no-hair conjecture has not been unambiguously proven, nor have its hypotheses been clearly stated, thus warranting further examination of the problem.

One particular work that stands out in this context is that of Wald [34], who did a comprehensive study of the late time evolution of anisotropic but homogeneous spaces with a cosmological constant. In this restricted setting, he was able to define the conditions for the cosmic no-hair conjecture to be satisfied by taking advantage of the Bianchi classification of homogeneous anisotropic metrics. Wald studied the time evolution of such metrics when the energy momentum tensor is the sum of two components: a cosmological constant and a term that satisfies the dominant and strong energy conditions. He found that, with the exception of the Bianchi IX, all other models asymptote to a de Sitter space within a time scale of $\sqrt{\frac{3}{\Lambda}}$. In the case of the Bianchi IX models, the future behavior depends on the relative sizes of the cosmological constant and the spatial curvature. Only when the latter exceeds the cosmological constant will the time evolution not lead to a de Sitter space.

Inflation is a beautiful solution to the horizon and flatness problems, but as already remarked in its early years, this is based on the assumption that the pre-inflationary state of the universe can be described by a homogeneous and isotropic Friedmann-Robertson-Walker (FRW) space. Since then, the question of whether an inflating region can continue to inflate if the ambient region is inhomogeneous has been explored by several authors for different pre-inflationary backgrounds. In a set of papers [35–37], Goldwirth and Piran sought to answer the question of whether a large inhomogeneity in the very early universe could prevent it from entering a period of inflation. In their work, inflation was not driven by a cosmological constant, but by an inflaton field. Their analysis is numerical and restricted to an inhomogeneous but isotropic and closed-universe background. They found that a large initial inhomogeneity could indeed suppress the onset of inflation, and that the inflaton field must have a suitable value over a region of several horizon sizes in order for inflation to start. This last finding raises the issue of an acausal initial conditions, although admittedly the required amount of fine-tuning will be below the required to explain the current observations in the absence of inflation. Other numerical simulations disagree with these results claiming that inhomogeneous backgrounds will have enough inflation to explain current observations [38, 39]. Analytical computations that use the long wavelength approximation seem to confirm that large inhomogeneities of the spatial curvature prevent the onset of inflation [40–42].

In this chapter we will not be able to conclusively settle this issue once and for all. Instead, our goal here is to study a particular problem that we believe captures some of the same physics, by playing local curvature effects against the might of the cosmological constant. The problem we consider is the classical evolution of a vacuum bubble in an inhomogeneous background, containing a cosmological constant and dust.

This background, which we will refer to as the Lemaître-Tolman-Bondi (LTB) spacetime (slightly generalized from the original form to allow for a positive cosmological constant), will be the simplest possible inhomogeneous space, spherically symmetric and with only one center [43–45]. The bubble will be created in a region of space that is expanding, but will encounter through its evolution regions of varying curvature. In a nutshell, the problem is that the critical size for bubble nucleation depends locally on the scale factor. Since this factor changes as a function of the position of the bubble, it is possible for a supercritical bubble to become subcritical. Our analysis will be confined to the evolution of the bubble, it will not address the interesting issue of tunneling probabilities in inhomogeneous backgrounds. This latter issue has been partially studied in [46]. Final conclusions can not be reached without knowing the effect of inhomogeneities on both tunneling transition rates as well as the bubble propagation.

3.1 Description of the Background on which the Bubble Propagates

A propagating bubble divides the space-time into three regions: outside, shell and inside. To give a proper description of this space-time in general relativity we will make use of the junction conditions, first presented by Israel [27] and extensively used since then by many authors. In particular, we will follow the implementation of this formalism developed by Berezin, Kuzmin and Tkachev [28].

The model we will study consists of a bubble of true vacuum propagating on a metastable vacuum whose energy-momentum tensor contains a higher cosmological constant and dust. In addition, we will assume that this outer space-time is asymptotically flat. The bubble is assumed to be a thin-shell, with a perfect-fluid energy-momentum tensor whose equation of state will be allowed to vary. The true vacuum will be assumed homogeneous and isotropic while the outside background will be assumed to be spherically symmetric about one point in space.

The line element of the outside region [47] is:

$$ds^2 = -dt^2 + \frac{[a(t,r) + ra'(t,r)]^2}{1 - \frac{r^2}{R^2(r)}} dr^2 + a^2(t,r) r^2 d\Omega_2. \tag{3.1}$$

The expansion parameter $a(t,r)$ is both a function of time and of the radial coordinate r. Partial derivatives with respect to the radial coordinate will be represented by a prime and partial derivatives with respect to time will be represented by a dot. The function $R(r)$ is an arbitrary function of the radial coordinate only and will be taken to be positive everywhere. This form of the outside metric allows us to investigate the effects of inhomogeneous backgrounds on the evolution of a bubble by making different choices of $R(r)$. Because it is our prejudice that curvature will interfere with the expansion of the bubble, when its value is comparable to the cosmological constant, we will particularly investigate $R(r)$ such that the curvature tends to zero for large radii but for small radius can overwhelm the effect of the cosmological constant.

The equations of motion for the expansion factor and the dust density $d(t,r)$, in units where $8\pi G = 1$, are:

$$\begin{aligned} \frac{\dot{a}^2(t,r)}{a^2(t,r)} + \frac{1}{a^2(t,r)R^2(r)} &= \frac{A}{a^3(t,r)} + \frac{\Lambda_{out}}{3}, && (3.2) \\ \frac{1}{3} d(t,r) a^2(t,r)(a(t,r) + ra'(t,r)) &= A. && (3.3) \end{aligned}$$

A is a constant. These equations reduce to the familiar Friedmann-Robertson-Walker equations in the limit where $R(r)$ is independent of the radial coordinate.

Besides choosing $R(r)$ the solution to the equations of motion will involve the choice of $a(t_0, r)$. To simplify our computations we will choose this function to be independent of the radial coordinate r.

The <u>bubble</u> will be assumed to be a thin-shell (described by a hypersurface Σ) and spherically symmetric. Its energy momentum tensor will be assumed to be of a perfect-fluid type: ${S_0}^0 = \sigma, {S_2}^2 = {S_3}^3 = P$, $P = w\sigma$, and with the metric:

$$ds^2|_\Sigma = -d\tau^2 + \rho^2(\tau) d\Omega_2. \tag{3.4}$$

The <u>interior of the bubble</u> will be assumed homogeneous and described by

$$ds^2 = -dT^2 + b^2(T)\left(\frac{dz^2}{1+z^2} + z^2 d\Omega_2\right), \tag{3.5}$$

with the following equation of motion for the scale factor:

$$\left(\frac{db}{dT}\right)^2 = \left(\frac{\Lambda_{in}}{3}\right) b^2(T) - 1. \tag{3.6}$$

We are assuming the inner space-time of the bubble to be open as derived from a tunneling process [48].

3.2 Junction Conditions

Israel junction conditions connect the three portions of the spacetime. The first condition requires that the metric be a continuous function at the junction. In terms of the coordinates of the outside(inside) region, the position of the hypersurface Σ will be given by $r = x(t)$ and $z = Z(T)$, respectively. The continuity of the metric at Σ requires:

$$\rho(\tau) = a(t, x(t))x(t) = b(T)Z(T), \tag{3.7}$$

$$d\tau = \sqrt{1 - \frac{b^2(T)}{1 + Z^2(T)} \left(\frac{dZ}{dT}\right)^2} \; dT, \tag{3.8}$$

$$dt = \frac{\sqrt{1 - x^2/R^2}}{\sqrt{-\dot{x}^2 (ax)_{,x}^{\,2} + 1 - x^2/R^2}} \; d\tau, \tag{3.9}$$

where $(ax)_{,x} \equiv (a'(t,r)r + a(t,r))|_{r=x(t)}$.

We will outline the derivation of the second junction condition, detailed in [28]. Once the continuous matching of the metrics is carried out, the metric on the whole manifold can be written in a general form:

$$ds^2 = dn^2 + \gamma_{ij}(x, n)dx^i dx^j, \tag{3.10}$$

where the junction surface Σ is given by $n = 0$. We now apply Einstein equations using thin-wall approximation. The Einstein equations on the shell take the form:

$$(\Gamma^n_{ij} - \gamma_{ij}\Gamma^n_{kl}\gamma^{kl})^+ - (\Gamma^n_{ij} - \gamma_{ij}\Gamma^n_{kl}\gamma^{kl})^- = S_{ij}, \tag{3.11}$$

where S_{ij} is the surface stress-energy tensor on the shell, + denotes the outer region, − the inner region, and we're using $8\pi G = 1$. The outer curvature tensor of the surface Σ is defined by:

$$K_{ij} \equiv -\mathcal{N}_{ij} = \Gamma^{n}_{ij}, \tag{3.12}$$

where $\mathcal{N}$ is the unit vector normal to the surface Σ. (3.11) can now be rewritten as:

$$[K^{j}_{i}] - \delta^{j}_{i}[K^{l}_{l}] = S^{j}_{i}, \tag{3.13}$$

where

$$[K^{j}_{i}] \equiv K^{j+}_{i} - K^{j-}_{i} \tag{3.14}$$

is the discontinuity of the outer curvature tensor.

Using this notation, the other components of the Einstein equation yield:

$$S^{j}_{i\,|j} + [T^{n}_{i}] = 0, \tag{3.15}$$

and

$$\{K^{i}_{j}\}S^{j}_{i} + [T^{n}_{n}] = 0, \tag{3.16}$$

where the vertical bar denotes covariant differentiation with respect to the metric on Σ, and

$$\{K^{i}_{j}\} \equiv \frac{1}{2}(K^{i+}_{j} + K^{i-}_{j}). \tag{3.17}$$

In the particular case of a spherical shell, which is our case of interest, we obtain from (3.13):

$$S^{0}_{0} = 2[K^{2}_{2}], \tag{3.18}$$

and

$$S^{2}_{2} = [K^{0}_{0}] + [K^{2}_{2}]. \tag{3.19}$$

Similarly, equations (3.15) and (3.16) now become:

$$\frac{dS_0^0}{d\tau}+\frac{2}{\rho}\frac{d\rho}{d\tau}(S_0^0-S_2^2)+[T_0^n]=0, \tag{3.20}$$

and

$$\{K_0^0\}S_0^0+2\{K_2^2\}S_2^2+[T_n^n]=0, \tag{3.21}$$

where we assume that the metric on the shell takes the form (3.5).

Berezin et al. [28] derive the general expressions for the components of the outside curvature tensor:

$$K_0^0 \;=\; -\frac{\gamma}{(\dot{\rho}^2-\Delta)^{1/2}}\left[\ddot{\rho}+\frac{1+\Delta}{2\rho}-\frac{\rho}{2}T_n^n\right], \tag{3.22}$$

$$K_2^2 \;=\; -\frac{\gamma}{\rho}(\dot{\rho}^2-\Delta)^{1/2}, \tag{3.23}$$

where

$$\Delta=g^{\alpha\beta}\rho_{,\alpha}\rho_{,\beta}\ \ , \tag{3.24}$$

$\gamma=+1$ when the radius is increasing in the direction of the outer normal to the surface Σ, and $\gamma=-1$ if the radius is decreasing. We can now see that equation (3.16) is a linear combination of equations (3.18) and (3.19).

To fully specify the dynamics, we not only need the dynamical equations but also the equation of state. Determining the relationship between σ and P on the shell from first principles is a difficult problem that requires a field-theoretic model for matter on either side. In the absence of a detailed understanding of this phase transition we will confine our study to perfect-fluid shells (${S_0}^0=\sigma, {S_2}^2={S_3}^3=P,\ P=w\sigma$), and explore various values of w.

We are now left with the system of equations:

$$\sigma = 2\,[{K_2}^2], \tag{3.25}$$

$$-P = [{K_0}^0] + [{K_2}^2], \tag{3.26}$$

$$\frac{d\sigma}{d\tau} = -\frac{2}{\rho}\frac{d\rho}{d\tau}(\sigma + P) - [{T_0}^n]. \tag{3.27}$$

The equations (3.25)-(3.27) are not independent, the latter is an integrability condition of the first two.

Using (3.22), (3.23), we obtain the outer curvature tensors for the outside and inside metric, as defined by (3.4) and (3.5).

<u>Outside Metric:</u>

$$\begin{aligned}
{K_2}^2 &= -\frac{\gamma_{out}}{\rho}(\dot{\rho}^2 - \Delta_{out})^{1/2}, \quad \text{where } \Delta_{out} = -1 + \rho^2\left(\frac{\Lambda_{out}}{3} + \frac{A}{a^3}\right),\\
{K_0}^0 &= -\frac{\gamma_{out}}{\sqrt{\dot{\rho}^2 - \Delta_{out}}}\left(\ddot{\rho} + \rho\left(-\frac{\Lambda_{out}}{3} + \frac{A}{2a^3}\right) + \frac{\rho}{2}\,\frac{d(t,r)\;\dot{x}^2\;(ax),_x^2}{(-\dot{x}^2(ax),_x^2 + 1 - x^2/R^2)}\right),\\
{T_0}^n &= -\frac{\dot{x}\;(ax),_x}{(-\dot{x}^2(ax),_x^2 + 1 - x^2/R^2)}d(t,x)\;\sqrt{1 - x^2/R^2}.
\end{aligned} \tag{3.28}$$

$\gamma_{out} = +1$ when the radius of the outside region is increasing in the outward direction normal to the surface Σ, and $\gamma_{out} = -1$ if the radius is decreasing.

Inside Metric:

$$\begin{aligned} {K_2}^2 &= -\frac{\gamma_{in}}{\rho}(\dot{\rho}^2 - \Delta_{in})^{1/2}, \quad \text{where } \Delta_{in} = -1 + \rho^2 \frac{\Lambda_{in}}{3}, \\ {K_0}^0 &= -\frac{\gamma_{in}}{\sqrt{\dot{\rho}^2 - \Delta_{in}}}\left(\ddot{\rho} - \rho\frac{\Lambda_{in}}{3}\right), \\ {T_0}^n &= 0. \end{aligned} \tag{3.29}$$

$\gamma_{in} = +1$ when the radius of the inside region is increasing in the outward direction normal to the surface Σ, and $\gamma_{in} = -1$ if the radius is decreasing.

Taking all this into account, we will study the evolution of the bubble by solving (3.25) and (3.27) simultaneously. In the absence of dust these equations can be written only in terms of $\rho(\tau)$, but this is no longer possible when dust is included.

Indeed, the equation (3.25) can be written as:

$$\dot{\rho}^2 = -1 + B^2\rho^2, \tag{3.30}$$

where

$$B^2 = \frac{\Lambda_{in}}{3} + \left(\frac{\sigma}{4} + \frac{1}{\sigma}\left(\frac{\Lambda_{out} - \Lambda_{in}}{3} + \frac{A}{a^3}\right)\right). \tag{3.31}$$

When solving (3.30) and (3.27) there is an additional point that we need to consider. Using the definition of outer curvature tensors given above, (3.25) can be written as:

$$\Delta_{out} - \Delta_{in} = \frac{\rho^2\sigma^2}{4} + \gamma_{out}\rho\sigma(\dot{\rho}^2 - \Delta_{out})^{1/2}. \tag{3.32}$$

Assuming $\sigma > 0$, which is our case of interest, we obtain the conditions:

$$\Delta_{out} - \Delta_{in} > \frac{\rho^2\sigma^2}{4} \qquad \text{if} \qquad \gamma_{out} = +1, \tag{3.33}$$

$$\Delta_{out} - \Delta_{in} < \frac{\rho^2\sigma^2}{4} \qquad \text{if} \qquad \gamma_{out} = -1. \tag{3.34}$$

Furthermore, defining:

$$\xi \equiv \frac{4(\Delta_{out} - \Delta_{in})}{\rho^2\sigma^2}, \tag{3.35}$$

and using (3.25), the following relationship holds:

$$\gamma_{in} \mid \xi + 1 \mid - \gamma_{out} \mid \xi - 1 \mid = 2. \tag{3.36}$$

Depending on the outer and inner geometry, and given the energy densities both inside and outside the bubble, there will only be a certain range of possible values for the energy density σ on the surface of the bubble consistent with (3.36).

3.3 Bubble Expansion in a Homogeneous Background

The study of the bubble evolution can be done in different sets of coordinates. The problem of interest is most conveniently analyzed in the coordinates of the outside background when dust is present. To familiarize ourselves with these coordinates we will devote this section to analyze a simpler problem. The simplification will come from restricting the outside background to be homogeneous ($R(r) = const$). First, we will redo the well studied motion of a vacuum shell in a cosmological constant background. Then we will add a dust energy density to the cosmological constant.

3.3.1 Homogeneous Background without Matter

The Israel junction conditions (3.25)-(3.27) tell us that it is consistent to have a vacuum shell (surface energy is constant and $w = -1$) in a transition that separates two de Sitter spaces with different values of the cosmological constant.

In terms of the intrinsic bubble coordinates, the equation (3.30) can be easily solved:

$$\rho(\tau) = \frac{1}{B}\cosh B\tau, \tag{3.37}$$

where in this case:

$$B^2 = \frac{\Lambda_{in}}{3} + \left(\frac{\sigma}{4} + \frac{\Lambda_{out} - \Lambda_{in}}{3\sigma}\right)^2, \tag{3.38}$$

regardless of the curvature of the outside background. The effect of this curvature only becomes manifest when we express the motion of the bubble in terms of the outside coordinates. In these coordinates the evolution of the position of the bubble is given by:

$$\frac{dx}{dt} = \frac{-(1 - \frac{x^2}{R^2})\sqrt{(\frac{\Lambda}{3} - \frac{1}{a^2R^2})} \pm \sqrt{(B^2a^2x^2 - 1)(B^2 - \frac{\Lambda}{3})(1 - \frac{x^2}{R^2})}}{a^2x(B^2 - \frac{1}{a^2R^2})}, \tag{3.39}$$

where the further assumption that $\Lambda_{in} = 0$ and $\Lambda_{out} = \Lambda$ has been made.

The evolution of the scale factor is given by:

$$\frac{\dot{a}^2}{a^2} + \frac{1}{a^2R^2} = \frac{\Lambda}{3}. \tag{3.40}$$

For times $t >> \frac{1}{H} = \sqrt{3/\Lambda}$, (3.39) and (3.40) reveal the following asymptotic behavior:

$$\begin{aligned}
a(t) &\rightarrow \frac{1}{2HR}\, e^{Ht}, \qquad \text{when} \quad a(0) = \frac{1}{HR}, \\
x(t) &\rightarrow R \sin\left(\frac{C}{R}\right) - O(e^{-Ht}), \qquad \text{if } R > 0 \text{ and finite,} \\
x(t) &\rightarrow \text{constant} + O(e^{-HT}), \qquad \text{if } R \rightarrow \infty.
\end{aligned} \tag{3.41}$$

Asymptotically the difference between the case with and without curvature is encoded in the dependence on $a(0)$. A space with positive curvature only makes sense if $a(0) \geq \frac{1}{RH}$. Once the initial value exceeds this critical value the space expands forever. The effect of the curvature becomes eventually negligible. Thus it is not surprising that the evolution of the bubble is similar in both instances. There is a difference in the possible asymptotic value that x can take; in the positive curvature case x always has to remain below R. The rate of the expansion is asymptotically given by B in the shell coordinates and by H in the outside coordinates.

In terms of the inside coordinates the motion of the bubble is given by:

$$Z(T) = \frac{1}{B}\sqrt{1 + B^2(T - T_0)^2}. \tag{3.42}$$

This expression can be derived from (3.7) and (3.8) assuming that $b(T_0) = 1$, which is a good assumption when $\Lambda_{in} = 0$. T_0 is the inside time at which the bubble is created. For late times the bubble propagates at the speed of light as expected [48].

Ultimately, we are always interested in the motion of the bubble as viewed by the observer inside the bubble. The moral of this example is that the motion, as viewed by the inside observer, is the same regardless of the amount of curvature outside the bubble.

The effects of curvature on the bubble propagation, as seen by the outside observer, are illustrated in Figures 3.1, 3.2 and 3.3. To simulate these evolutions we have chosen the following values for the parameters, in units of $8\pi G = 1$:

$$\begin{aligned} \Lambda &= 3 \times 10^{-5}, \\ a_{init} &= 5, \\ \gamma_{out} &= \gamma_{in} = +1, \\ \sigma_{init} &= 10^{-3}. \end{aligned} \tag{3.43}$$

These values can't all be chosen independently since they have to satisfy the condition (3.36) that yields:

$$\sigma \leq 2\sqrt{\frac{\Lambda}{3}} = 6.3 \times 10^{-3}. \tag{3.44}$$

Also, from the equation (3.39) the lower and the upper bound on x are:

$$\frac{1}{aB} \leq x \leq R. \tag{3.45}$$

We have chosen the initial size of the bubble in accordance with this range. An example of the Wolfram Mathematica code used to generate the plots can be found in Appendix B.

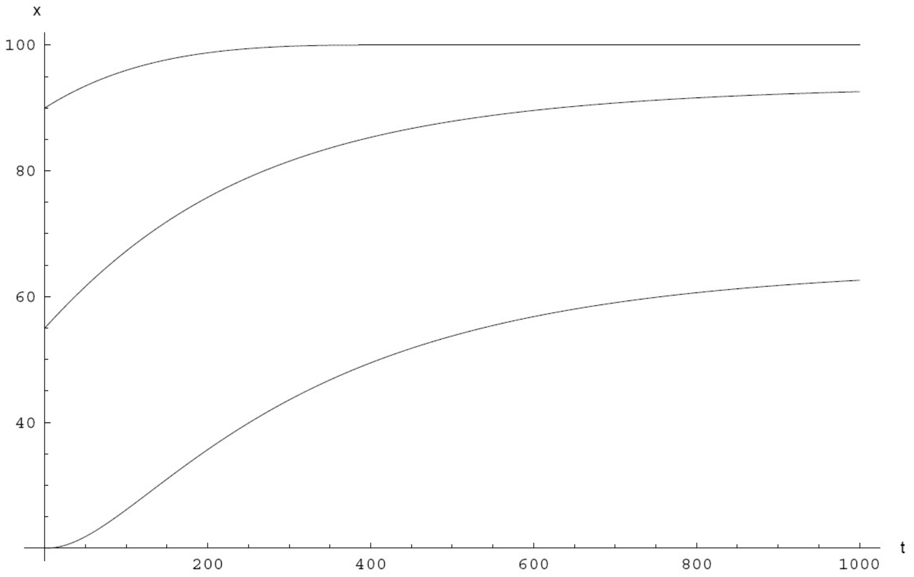

Figure 3.1: Time evolution of the bubble in the outside coordinates, $x[t]$, for several initial sizes, $x_{init} = 20, 55, 90$. The background is assumed homogeneous ($R = 100$) and without matter.

In particular, Figure 3.1 shows the evolution of the bubble in the outside coordinates for various initial sizes. Note that the maximum size of the bubble in these coordinates corresponds to the limit $x = R$.

Figure 3.2 shows the effects of curvature on bubble propagation by comparing evolutions of bubbles with the same initial size x_{init}, but in different curvature backgrounds. We see that more curvature corresponds to a slower evolution of the bubble in the outside coordinates; however, the corresponding

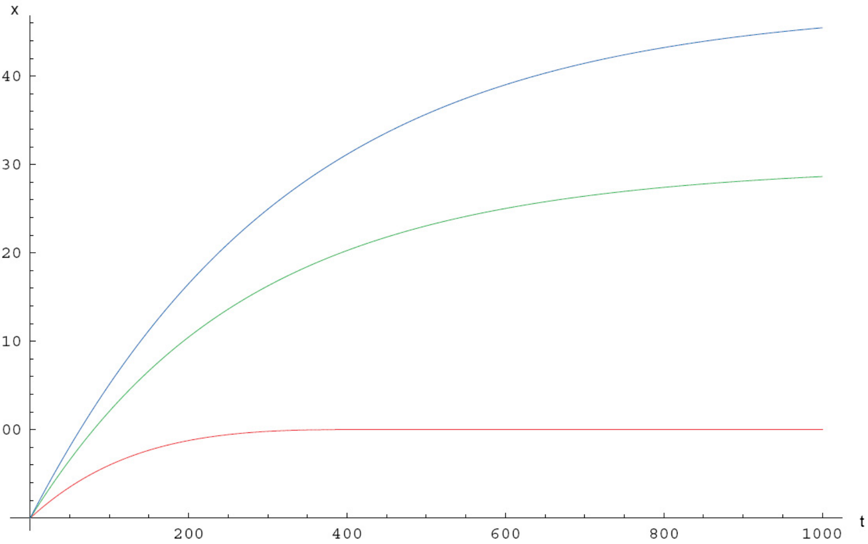

Figure 3.2: Time evolution of the bubble in the outside coordinates, $x[t]$, in homogeneous backgrounds without matter. Colors correspond to different choices of R; $R = 100$ red, $R = 150$ green, $R = \infty$ blue.

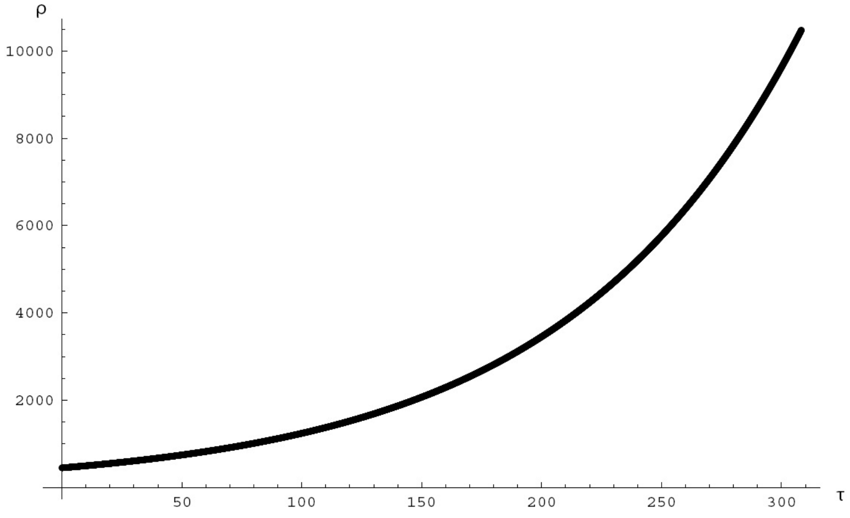

Figure 3.3: Time evolution of the bubble in the coordinates of the bubble, $\rho[\tau]$, in homogeneous backgrounds without matter (same as in Figure 3.2).

bubble evolution $\rho[\tau]$ in the bubble coordinates is exactly the same, irrespective of the amount of background curvature, and it is shown in Figure 3.3.

In addition, one might wonder what would happen if we did not assume the bubble to be a vacuum bubble, namely if $w \neq -1$. Then the evolution of the energy density σ on the bubble is governed by (3.27). In the absence of dust on the outside the solution to this equation is:

$$\sigma = \frac{\xi}{\rho^{2(1+w)}}, \tag{3.46}$$

where ξ is a constant. When substituting this solution on (3.25) we obtain the following equation for $\rho(\tau)$

$$\dot{\rho}^2 = -1 + \left(\frac{\xi}{4\rho^{(1+2w)}} + \frac{\Lambda}{3\xi}\,\rho^{3+2w} \right)^2 . \tag{3.47}$$

For ρ large, the solution to this equation takes the form:

$$\rho(\tau) \sim \frac{\rho(\tau_0)}{\left[1 - (1+2w)\frac{\Lambda}{3\xi}\rho(\tau_0)^{1+2w}(\tau - \tau_0)\right]^{1/(1+2w)}}. \tag{3.48}$$

This analysis of the asymptotic behavior is also captured in the results plotted in Figures 3.4 and 3.5.

Figure 3.6 depicts the corresponding bubble evolution in the outside coordinates, $x[t]$. We see that for bigger w, $x[t]$ grows faster. This can be understood from equations (3.38) and (3.39). As σ goes to zero, B rapidly grows, which in turn leads to the greater contribution of the second, positive term, over the first, negative term in the evolution of $x[t]$.

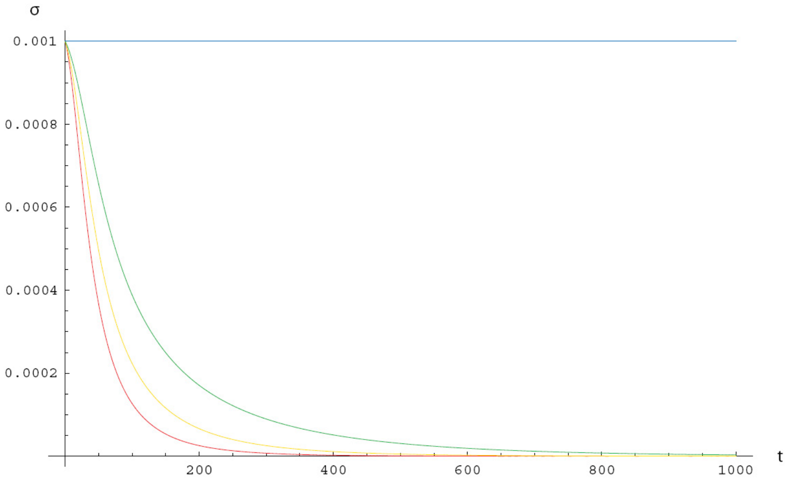

Figure 3.4: Time evolution of the surface energy density $\sigma[t]$ on the bubble. The background is assumed homogeneous ($R = 100$) and without matter. Colors correspond to different equations of state; $w = 1/3$ red, $w = 0$ yellow, $w = -1/3$ green, $w = -1$ blue.

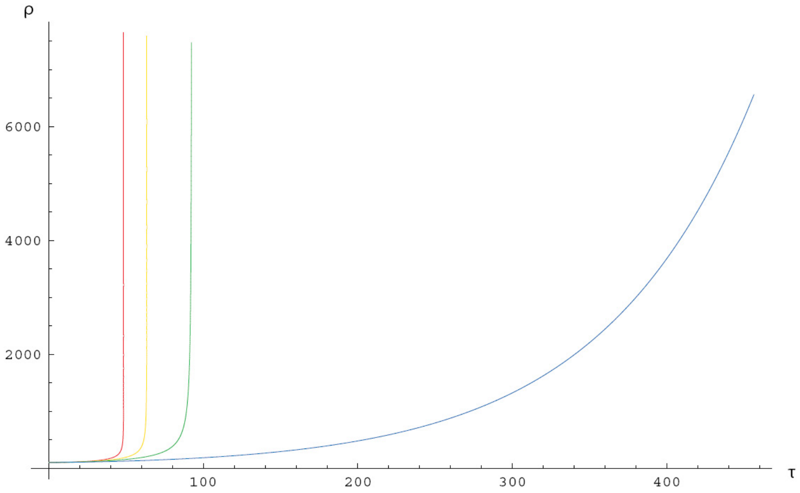

Figure 3.5: Time evolution of the bubble in the coordinates of the bubble, $\rho[\tau]$. The background is assumed homogeneous ($R = 100$) and without matter. Colors correspond to different equations of state; $w = 1/3$ red, $w = 0$ yellow, $w = -1/3$ green, $w = -1$ blue.

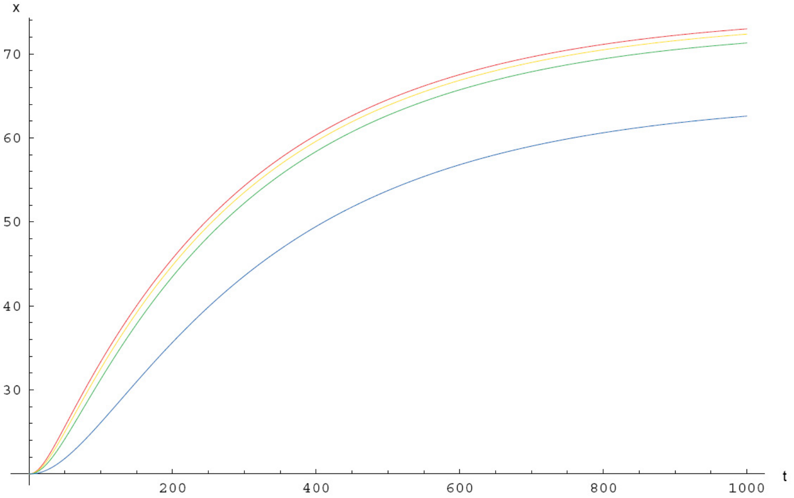

Figure 3.6: Time evolution of the bubble in the outside coordinates, $x[t]$. The background is assumed homogeneous ($R = 100$) and without matter. $x_{init} = 20$. Colors correspond to different equations of state; $w = 1/3$ red, $w = 0$ yellow, $w = -1/3$ green, $w = -1$ blue.

3.3.2 Homogeneous Background with Matter

To study the evolution of the bubble in a space that might contract we have to modify the outside energy density. One option is to introduce matter. In this instance the evolution of the scale parameter is given by

$$\dot{a}^2 + \frac{1}{R^2} - \frac{\Lambda}{3}a^2 - \frac{A}{a} = 0. \tag{3.49}$$

If $A \leq \frac{1}{R^3}\sqrt{\frac{4}{9\Lambda}}$ and $a(0)$ is small enough, the expansion of the universe will reverse into contraction. It is interesting to study the evolution of bubbles in different cases.

With this new form of outside energy density, however, it is no longer consistent with the matching conditions to have a constant surface energy density on the bubble, not even when $\sigma + P = 0$. The evolution will be given by the equations:

$$\frac{dx}{dt} = \frac{-\left(1-\frac{x^2}{R^2}\right)\frac{\dot{a}}{a} \pm \sqrt{\left(1-\frac{x^2}{R^2}\right)\left(a^2B^2x^2-1\right)\left(B^2-\left(\frac{\Lambda}{3}+\frac{A}{a^3}\right)\right)}}{xa^2(B^2-\frac{1}{a^2R^2})} \tag{3.50}$$

$$\frac{d\sigma}{dt} = -2\left(\frac{\dot{a}}{a}+\frac{\dot{x}}{x}\right)(\sigma+P) + \frac{\dot{x}}{\sqrt{-\dot{x}^2a^2+1-\frac{x^2}{R^2}}}\frac{3A}{a^2}, \tag{3.51}$$

$$B = \frac{\sigma}{4} + \frac{1}{\sigma}\left(\frac{\Lambda}{3}+\frac{A}{a^3}\right). \tag{3.52}$$

As in the previous section, in order to solve these equations an assumption about the equation of state on the bubble is needed. We make the assumption that the shell is made of a perfect fluid with equation of state $P = w\,\sigma$, and explore several values for w. For the dust energy to be comparable to the cosmological constant at early times, we choose

$$A = 10^{-4}, \tag{3.53}$$

in Planck units. The critical curvature which is the minimal curvature needed for the space to turn around and eventually collapse is given by:

$$R_{cr} = \left(\frac{9\Lambda A^2}{4}\right)^{-1/6} = 107. \tag{3.54}$$

The position of the maximum of the potential $V[a]$ is given by:

$$a_{max} = \left(\frac{3A}{2\Lambda}\right)^{1/3} = 1.7. \tag{3.55}$$

In our simulations we choose the initial value of the scale factor a to be $a_{init} = a(0) = 1$.

The outside background geometry will be completely specified once we choose the amount of curvature. We will consider several cases.

3.3.2.1 $R > R_{cr}$

For $R > R_{cr}$ the universe will always expand. If at the instant the bubble is created $a(0)$ is to the left of the maximum of the potential, then the universe will experience a period of slower growth until it eventually goes over the maximum and the expansion becomes dominated by the cosmological constant.

We will now investigate bubble propagation on such background. We are again assuming that the inside region has zero energy density, and that $\gamma_{out} = \gamma_{in} = +1$. In this case, the condition (3.36) yields:

$$\sigma \leq 2\sqrt{\frac{\Lambda}{3} + \frac{A}{a^3}}. \tag{3.56}$$

This constraint will be the strongest as $a \to \infty$, when, as is the case without matter, it reduces to:

$$\sigma \leq 6.3 \times 10^{-3}. \tag{3.57}$$

Once again, we choose:

$$\sigma_{init} = 10^{-3}, \tag{3.58}$$

where σ_{init} is given in Planck units. The initial size of the bubble is taken in accordance with the range (3.45).

We will compare the evolution for several equations of state on the surface of the bubble. Decreasing R (and therefore increasing the curvature of the space) will have the effect of slowing down the evolution, as long as $R > R_{cr}$.

First let us consider the case with very little curvature, $R = 500$. Figure 3.7 shows the time evolution of bubbles of several initial sizes in the outside coordinates. In most cases bubbles grow without reaching the upper bound, $x = R$. Smaller w slows down the expansion rate, and in particular, the choice of $w = -1$ soon leads to a contracting bubble in the outside coordinates. Depending on the initial size of the bubble, $w = -1$ bubbles either reach the lower bound, $x = \frac{1}{aB}$, which results in the breakdown of the simulation, or eventually stabilize and stop contracting.

Time evolution in the coordinates on the bubble (Figure 3.8) reveals behavior similar to the case without matter. Namely, for the bubbles that do survive, the evolution is slower than in the case without matter, but the overall qualitative behavior stays the same.

Next we turn to the case with more curvature, but still such that $R > R_{cr}$. From Figure 3.9 we see that in most cases bubbles again grow, but now they asymptote to the upper bound, $x = R$. The corresponding bubble evolution in the coordinates on the bubble is shown in Figure 3.10. The overall effect of more curvature is a further slowdown in the time evolution of the bubbles.

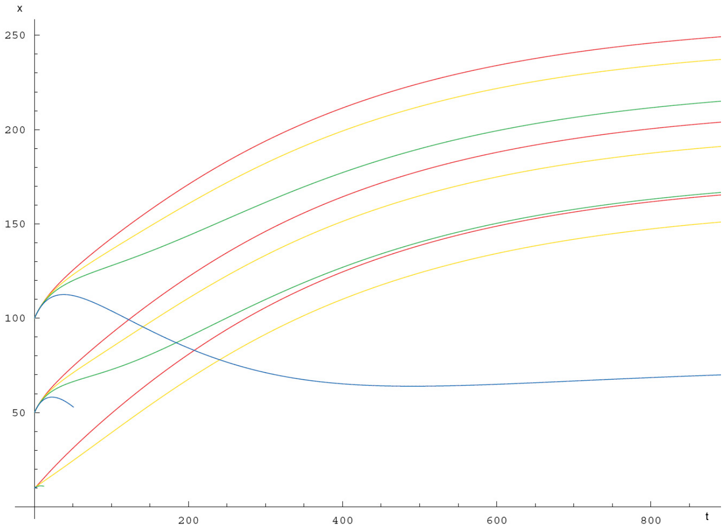

Figure 3.7: Time evolution of the bubble in the outside coordinates, $x[t]$, for several initial sizes, $x_{init} = 10, 50, 100$. The background contains homogeneous curvature ($R = 500$) and matter ($A = 10^{-4}$). Colors correspond to different equations of state; $w = 1/3$ red, $w = 0$ yellow, $w = -1/3$ green, $w = -1$ blue.

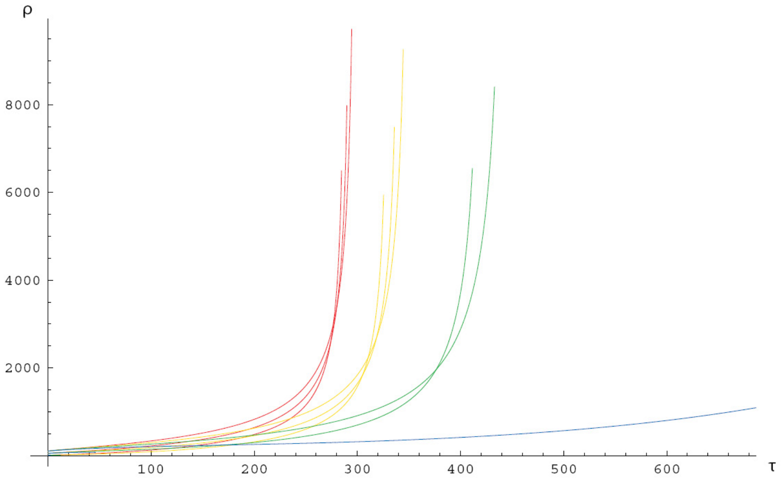

Figure 3.8: Time evolution of the bubble in the bubble coordinates, $\rho[t]$, for the same background conditions as in Figure 3.7. Colors correspond to different equations of state; $w = 1/3$ red, $w = 0$ yellow, $w = -1/3$ green, $w = -1$ blue.

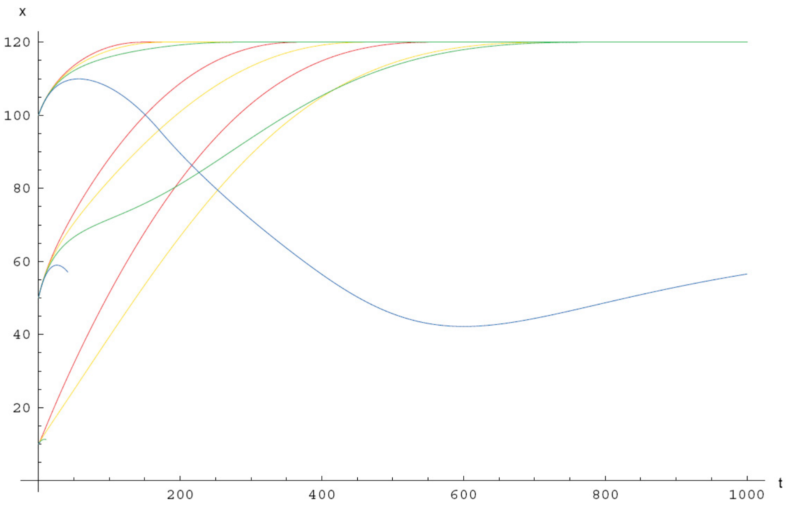

Figure 3.9: Time evolution of the bubble in the outside coordinates, $x[t]$, for several initial sizes, $x_{init} = 10, 50, 100$. The background contains homogeneous curvature ($R = 120$) and matter ($A = 10^{-4}$). Colors correspond to different equations of state; $w = 1/3$ red, $w = 0$ yellow, $w = -1/3$ green, $w = -1$ blue.

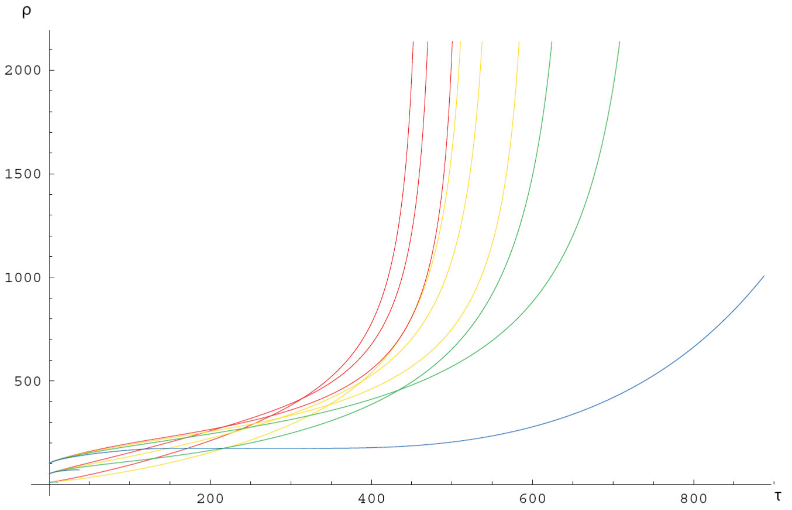

Figure 3.10: Time evolution of the bubble in the bubble coordinates, $\rho[t]$, for the same background conditions as in Figure 3.9. Colors correspond to different equations of state; $w = 1/3$ red, $w = 0$ yellow, $w = -1/3$ green, $w = -1$ blue.

3.3.2.2 $R < R_{cr}$

For curvature greater than the critical value (i.e. $R < R_{cr}$) the space will eventually collapse. To investigate this case we choose $R = 100$. The evolution of the scale factor is shown in Figure 3.11.

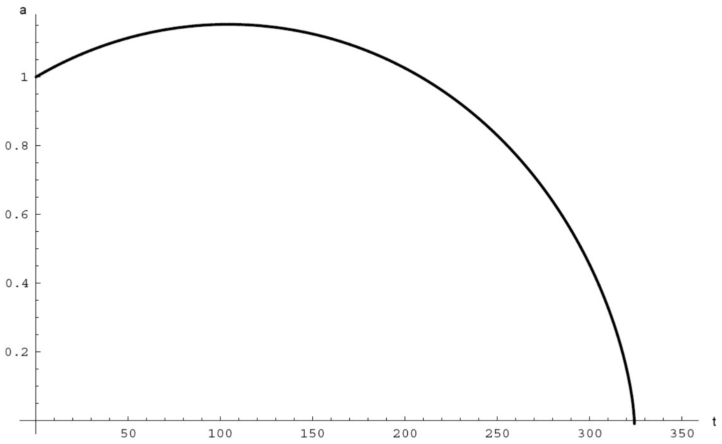

Figure 3.11: Time evolution of the scale factor $a[t]$ for $R = 100$. ($\Lambda = 3 \times 10^{-5}, A = 10^{-4}$.)

In the outside coordinates, the time evolution of most bubbles will once again lead to the upper bound, $x = R$ (Figure 3.12). Bubbles with $w = -1$ contract and hit the lower bound $x = \frac{1}{aB}$, which stops their further evolution.

Figure 3.13 reveals corresponding behavior in the coordinates on the bubble. Bubbles which do not hit the bound $x = \frac{1}{aB}$ eventually collapse along with the collapse of the space itself.

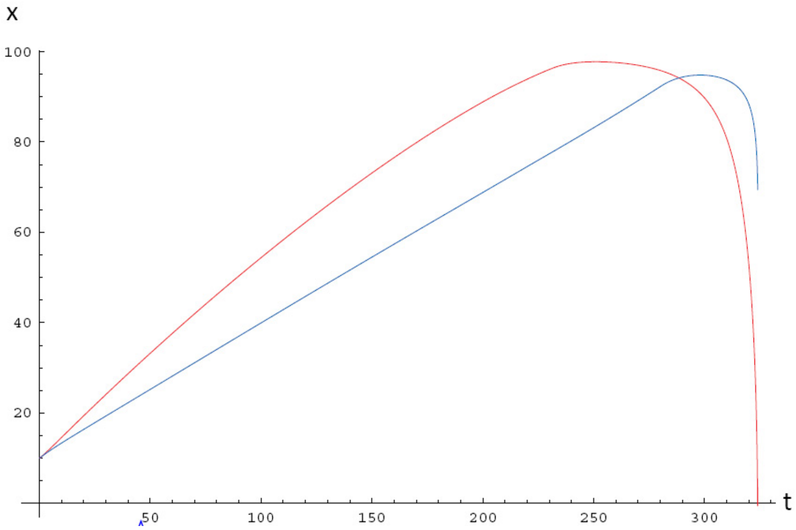

Figure 3.12: Time evolution of the bubble in the outside coordinates, $x[t]$, for crunching background (Figure 3.11). $x_{init} = 10$. $R = 100$. Colors correspond to different equations of state: $w = 1/3$ red, $w = 0$ blue.

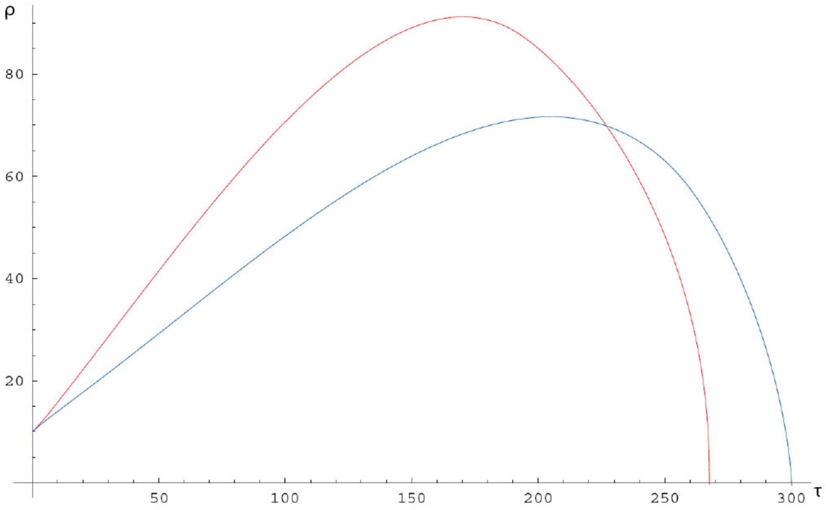

Figure 3.13: Time evolution of the bubble in the bubble coordinates, $\rho[t]$, for crunching background (Figure 3.11). $x_{init} = 10$. $R = 100$. Colors correspond to different equations of state; $w = 1/3$ red, $w = 0$ blue.

3.4 Bubble Expansion in Inhomogeneous Background

3.4.1 Generating a Curvature Profile

In order to generate an inhomogeneous curvature profile, we choose:

$$R(r) = (\alpha r + \beta R_{cr}) \left(1 \pm \frac{1}{\gamma + (\delta - r)^2} \right). \tag{3.59}$$

$\alpha > 0$ ensures that as $r \longrightarrow \infty$ we have an asymptotically flat space. Choosing $\beta > 1$ will allow us to generate a sharp drop in the function $R(r)$, for the cases where the minus sign is chosen. The position and the width of the extremum will be regulated by the parameter δ, and the depth/height by γ. Since we do not want our space to crunch anywhere, we will require $R(r) > R_{cr}$ for all r.

Furthermore, we want to make sure to satisfy the weak energy condition, namely that the matter density stays positive:

$$d(t,r) = \frac{3A}{a^2(t,r)(a(t,r) + ra'(t,r))}. \tag{3.60}$$

Since A is positive definite, this gives us a condition:

$$a(t,r) + ra'(t,r) > 0. \tag{3.61}$$

This means that $a(r)$ should nowhere fall faster than $1/r$.

3.4.2 Examples

As an example, we first choose the minus sign in $R(r)$, with $\alpha = 0.1$, $\beta = 3$ and $\delta = 20$. In order for R to stay above R_{cr}, in this case we need $\gamma > 1.5$. In addition, numerical simulations show that to satisfy the weak energy condition, $\gamma \geq 2.9$, and since we'd like to investigate the sharpest possible profile, we choose $\gamma = 2.9$. Therefore, our $R(r)$ takes the form:

$$R(r) = (0.1r + 3R_{cr}) \left(1 - \frac{1}{2.9 + (20 - r)^2}\right). \tag{3.62}$$

This choice of the function $R(r)$ generates a profile in the evolution of the scale factor $a(r, t)$, as shown in Figure 3.14. We will compare evolution of a bubble in such background with evolution in a curvature background without a profile, namely, $R(r) = (0.1r + 3R_{cr})$. The two choices of $R(r)$ are shown in Figure 3.15.

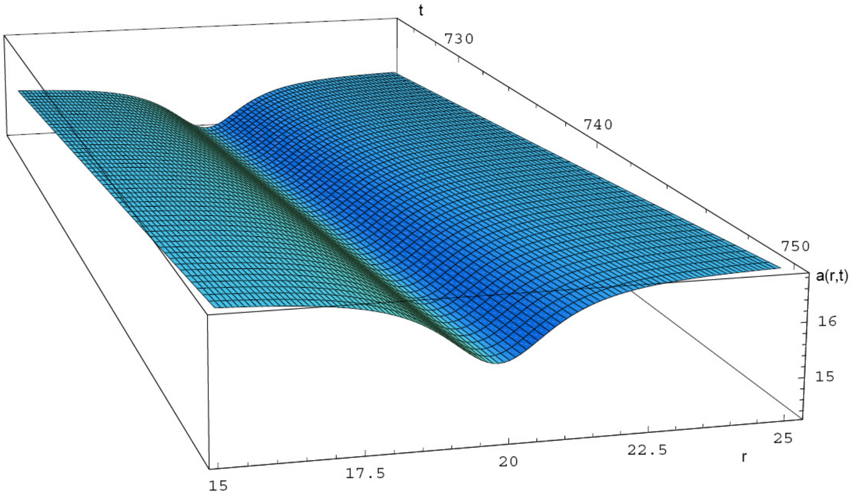

Figure 3.14: $a(r, t)$ as a consequence of the profile (3.62), depicted in red in Figure 3.15.

The resulting bubble evolutions are shown in Figures 3.16 and 3.17. We see that even though in the outside coordinates bubble evolution is greatly affected by the curvature profile, such effect is absent for the bubble evolution in the coordinates on the bubble.

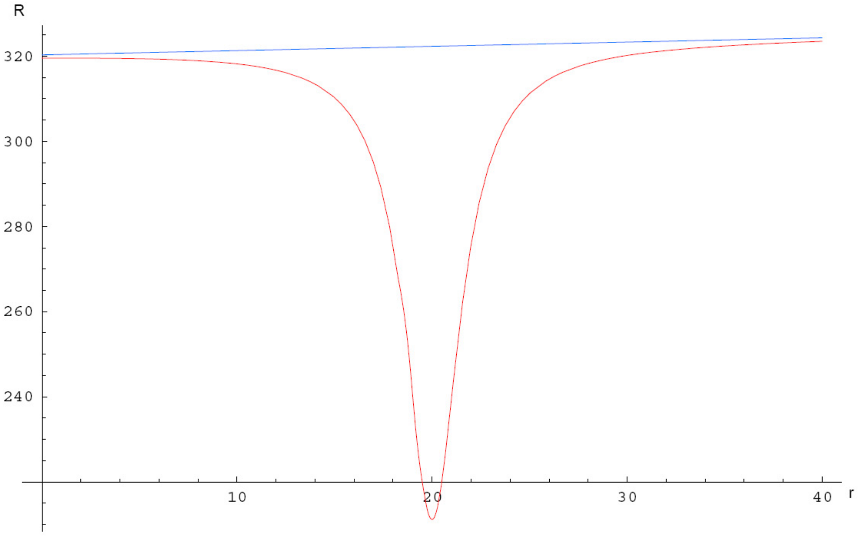

Figure 3.15: First example of an inhomogeneous background: Two choices of $R(r)$.

For comparison, we will also choose $R(r)$ with the plus sign, and $\alpha = 0.1$, $\beta = 2$,$\gamma = 0.7$ and $\delta = 20$:

$$R(r) = (0.1r + 2R_{cr}) \left(1 + \frac{1}{0.7 + (20 - r)^2} \right). \tag{3.63}$$

This results in a profile for $a(r,t)$ shown in Figure 3.18. We will compare the effects of this profile with a nearly constant curvature, shown in Figure 3.19. The corresponding bubble evolution is shown in Figures 3.20 and 3.21.

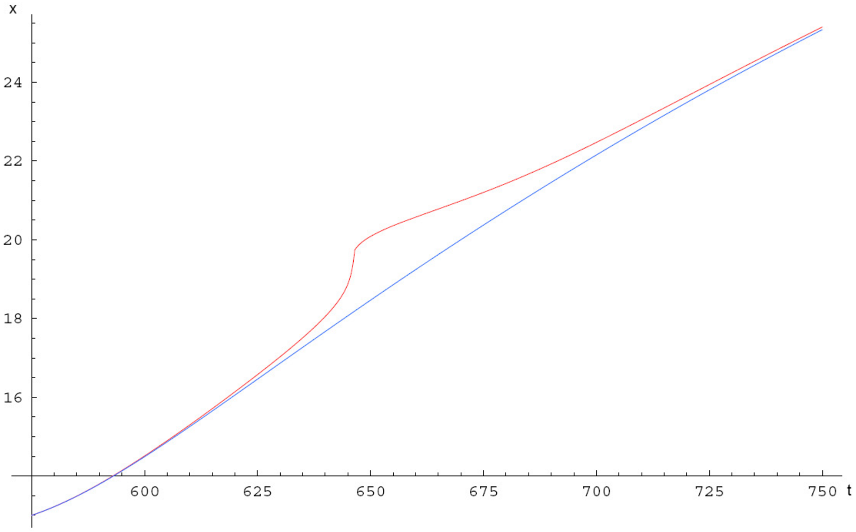

Figure 3.16: Evolution of bubbles in outside coordinates, $x(t)$, for two curvature profiles shown in Figure 3.15.

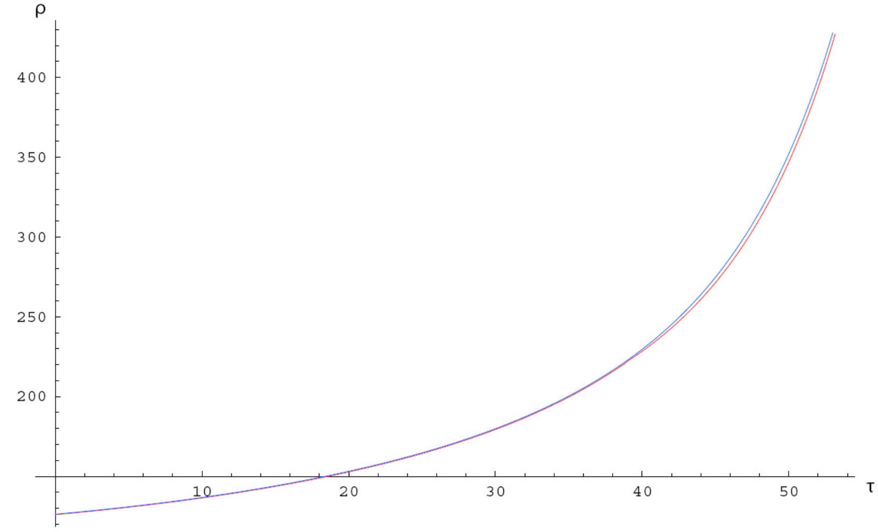

Figure 3.17: Evolution of bubbles in bubble coordinates, $\rho(\tau)$, for two curvature profiles shown in Figure 3.15.

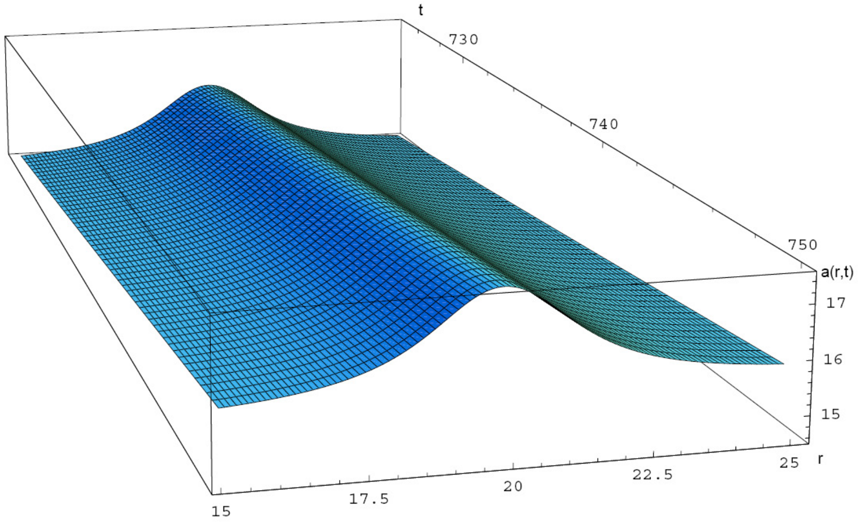

Figure 3.18: $a(r,t)$ as a consequence of the profile (3.63), depicted in red in Figure 3.19.

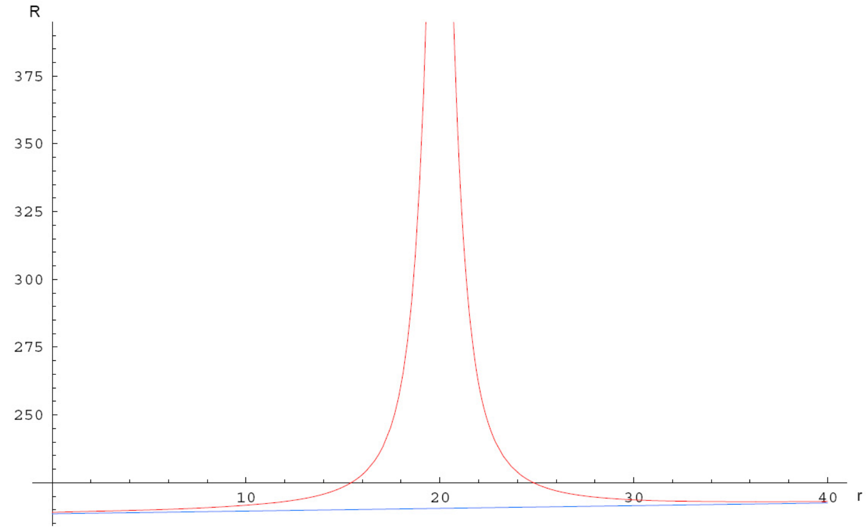

Figure 3.19: Second example of an inhomogeneous background: Two choices of $R(r)$.

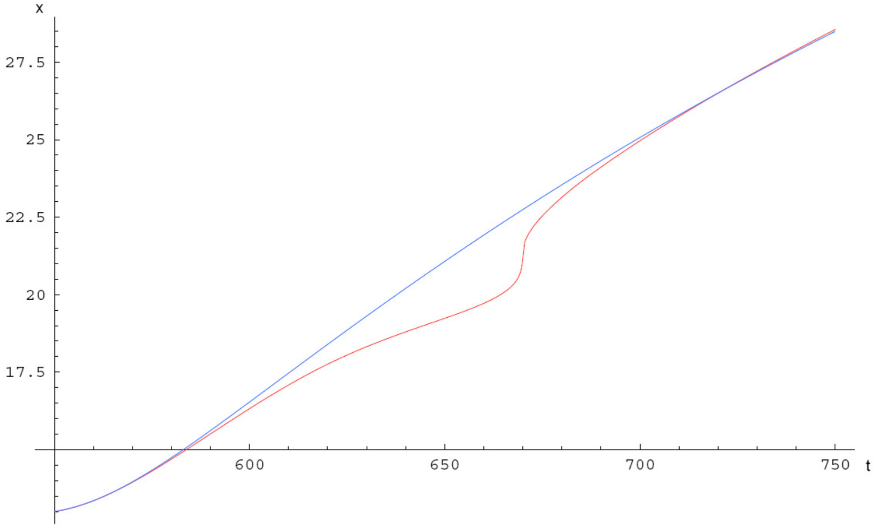

Figure 3.20: Evolution of bubbles in outside coordinates, $x(t)$, for two curvature profiles shown in Figure 3.19.

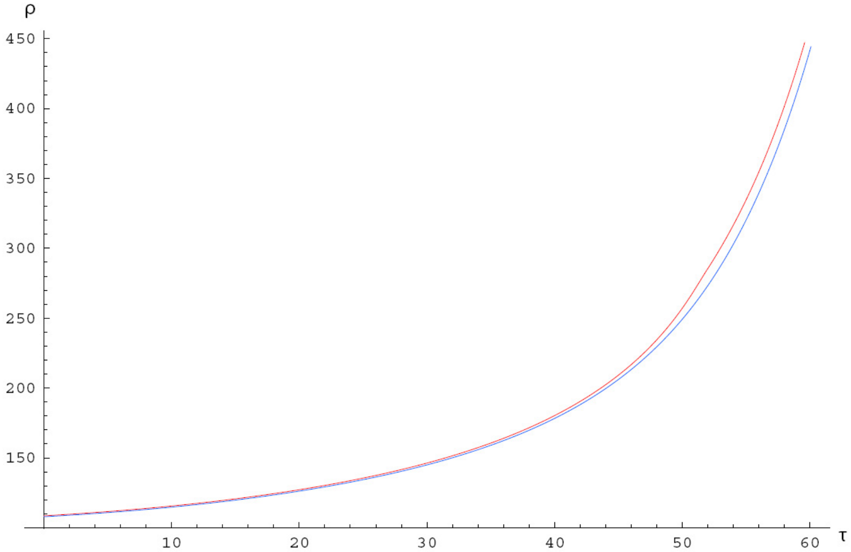

Figure 3.21: Evolution of bubbles in bubble coordinates, $\rho(\tau)$, for two curvature profiles shown in Figure 3.19.

3.5 Conclusions

We have investigated the propagation of vacuum bubbles on different backgrounds, always including a cosmological constant. We find that the effects of curvature can significantly change the propagation of a bubble from the point of view of the outside coordinates. However, this is not the case when the evolution is studied in terms of the more physically relevant coordinates on the shell, or its interior.

Namely, for cases without matter, we find that the evolution of a bubble in the coordinates on the bubble is completely unaffected by the curvature of the background. Once we introduce matter in the equations, we find that more curvature will lead to a slower time evolution of the bubble in the coordinates on the bubble, but the functional form remains the same. Furthermore, we looked at several equations of state on the bubble and found that greater the w, faster the bubble evolution is. In particular, for $w = 1/3, 0, -1/3$ bubble expansion diverges from the point of view of the bubble coordinates. In the presence of matter we also observe that some bubbles, with an equation of state close to $w = -1$, disappear.

In addition, for the examples of inhomogeneous curvature background studied, effects of inhomogeneity are negligible from the point of view of the observer on the bubble. It is important to note, however, that the weak energy condition (3.61) considerably restricts the sharpness of the allowed inhomogeneity profiles.

Chapter 4

The Energy Density of "Wound" Fields in a Toroidal Universe

In this chapter we present a model for a novel type of contribution to the present energy density of the universe which redshifts like $1/a^2$ and contributes to the present energy density at the level of roughly one percent.

We assume a flat universe with the spatial topology of a torus. The physical size of the torus at the onset of inflation is such that the minimum amount of inflation, needed to solve the horizon and flatness problems, leads to the lower bound on the present size of a toroidal universe, obtained by the search for "circles in the sky" [49]. Other bounds on the topology of the universe are available from the CMB fluctuations [50], as well as from galactic methods [51, 52].

In addition to the inflaton and conventional low energy states, we assume that the matter content has at least three massless angle-valued fields, θ_i, similar to axions. One crucial assumption will be the existence of a non-trivial topological configuration for these fields.

The model will lead to the existence of a component in the energy density that scales like $1/a^2$, and in the Friedmann equation mimics a negative spatial curvature term. However, unlike the curvature term, it does not modify the relation between the angular and the radial distance from what it is in flat space [53].

The motivation for this model comes from the fact that the present data, as best we can tell, does not exclude a contribution of a percent or so to the present energy density that could arise from such a construction, and therefore warrants some exploration.

We will begin by clearly stating the various assumptions and then describe how they can lead to a contribution of the order of a percent to the total energy density of the present universe.

4.1 Setup of the Model

In this section we will present the setup of fields which will lead to a component of the energy density of the universe scaling like $1/a^2$.

Our first assumption is that the universe is spatially flat with the topology of a torus. For simplicity, we will take the torus to be a cube with opposite sides identified. The coordinate distance between opposite sides of the cube is L. We will denote the three cycles of the torus by:

$$x_i = \frac{L}{2\pi}\chi_i, \tag{4.1}$$

where the χ_i are angles.

We will also assume the existence of three minimally coupled scalar fields, φ_i where $i = 1, 2, 3$ which span a torus in field space. The three cycles of the field-space torus have linear sizes f_i:

$$\varphi_i = \frac{f_i}{2\pi}\theta_i, \tag{4.2}$$

where the θ_i are angle valued fields, and the "decay constants" f_i are tunable parameters (like L).

These scalar fields are assumed to couple to matter through their derivatives[1] and that no potential is generated for these fields, i.e. the Lagrangian and the quantum dynamics that it generates, is invariant under the following transformations:

$$\theta_i \rightarrow \theta_i + c_i, \tag{4.3}$$

where c_i are (space-time independent) constants. These scalars can be thought of as massless axions.

We want to briefly address the question of whether these massless scalars could generate long range forces that would rule them out experimentally. A simple answer to such concern would be to require that they do not couple directly to the low energy degrees of freedom, except through gravity.

The equations of motion for the scalar fields in a Friedmann-Robertson-Walker (FRW) flat universe are:

$$\ddot{\theta}_i + 3\frac{\dot{a}}{a}\dot{\theta}_i - \frac{\nabla^2\theta_i}{a^2} = 0, \tag{4.4}$$

---

[1] The assumption that the φ_i are minimally coupled scalars ensures that the gravitational coupling of these scalars to matter is also through derivatives.

where the FRW metric we use is:

$$ds^2 = -dt^2 + a^2(t)\delta_{ij}dx^i dx^j. \tag{4.5}$$

Next, we choose as solution of equations (4.4) a topologically non-trivial configuration for the scalar fields:

$$\theta_i = w_i \chi_i, \tag{4.6}$$

where w_i corresponds to a winding number for each angular field around its respective cycle.

Now let us turn to the consequences of this setup.

4.2 $T_{\mu\nu}$ and the Isotropy of the Microwave Background

The components of the energy-momentum tensor, $T_{\mu\nu}$, associated with this solution are:

$$T^{(i)}_{00} = \frac{1}{2}\left(\frac{f_i w_i}{L_i a}\right)^2, \tag{4.7}$$

$$T^{(i)}_{ii} = \frac{1}{2}\left(\frac{f_i w_i}{L_i}\right)^2, \tag{4.8}$$

$$T^{(i)}_{jj} = -\frac{1}{2}\left(\frac{f_i w_i}{L_i}\right)^2, \tag{4.9}$$

where $i, j = 1, 2, 3$ and $j \neq i$.

We see that if one allows for different values for the "decay constants", f_i, in order to respect the stringent limit of one part in 10^5 on the isotropy of the microwave background, the sizes, L_i, of the cycles of the spatial torus must satisfy:

$$\frac{L_1}{w_1 f_1} = \frac{L_2}{w_2 f_2} = \frac{L_3}{w_3 f_3}. \tag{4.10}$$

Since we decided for simplicity to choose the spatial topology of the universe to be a torus with three cycles of same size, from now on we will assume that our scalar fields have the same "decay constants" $f_1 = f_2 = f_3 = f$ and winding numbers $w_1 = w_2 = w_3 = w$. This very special choice of a background solution for the θ_i, will ensure that we comply with the isotropy of the microwave background.

4.3 Contribution to the Energy Density

With the above assumptions, we see from (4.7) that the energy density, ρ_w, stored in this configuration of scalar fields is:

$$\rho_w = \frac{\nabla_i \varphi_j \nabla^i \varphi_j}{2a^2} = \frac{3w^2 f^2}{2L^2 a^2}. \tag{4.11}$$

The same dependence of the energy density on the scale factor can be obtained for an ideal fluid with the following equation of state:

$$P = -\frac{1}{3}\rho. \tag{4.12}$$

Namely, the energy conservation law for the FRW metric gives:

$$\frac{d\rho}{dt} + \frac{3\dot{a}}{a}(p + \rho) = 0, \tag{4.13}$$

which, assuming an equation of state of an ideal fluid, $p = \alpha\rho$, gives:

$$\rho \propto a^{-3-3\alpha}. \tag{4.14}$$

Therefore, our case corresponds to $\alpha = -1/3$.

It is interesting to note that this equation lies at the boundary between equations of state that lead to an accelerating universe and the ones that lead to the decelerating one. We can see that from the Friedmann equation, which governs the expansion of the universe and, like the energy conservation law (4.13), can be obtained from the Einstein equations.

$$\dot{a}^2 + K = \frac{8\pi G\rho a^2}{3} \tag{4.15}$$

Solving the Friedmann equation, (4.15), in the case $K = 0$ and assuming ideal fluid gives:

$$\begin{aligned} a \propto & t^{\frac{2}{3}\frac{1}{1+\alpha}} && \text{for} \quad \alpha \neq -1, \\ a \propto & \exp(Ht) && \text{for} \quad \alpha = -1, \end{aligned} \tag{4.16}$$

where H is the Hubble constant, given by:

$$H = \sqrt{\frac{8\pi G\rho_V}{3}}, \tag{4.17}$$

and ρ_V is the vacuum energy density, $\rho_V = 8\pi G\Lambda$.

For $\alpha = -1/3$ this corresponds to $a \propto t$. However, we will see that in our model the energy stored in the "wound" scalar fields has never been the dominant component of the energy density of the universe. Therefore that component of the energy density does not affect the leading characteristics of the expansion of the universe.

Even though this energy density redshifts like the spatial curvature contribution to the Friedmann equation, it does not alter the relation between angular and radial distances from their flat space behavior [53].

In particular, the luminosity distance, which is a common observable parameter, is defined as:

$$d_L \equiv \left(\frac{L}{4\pi l}\right)^{1/2}, \tag{4.18}$$

where L is the absolute luminosity, and l is the apparent luminosity, corresponding to the power received per unit area of the mirror.

Since the apparent luminosity of a source at radial coordinate r with a redshift z is given by [54]:

$$l = \frac{L}{4\pi r^2 a^2(t_0)(1+z)^2}, \tag{4.19}$$

where subscript 0 denotes present quantities, it follows that:

$$d_L = a(t_0) r (1+z). \tag{4.20}$$

A light ray which leaves a distant source from a radial coordinate r at time t_1 will arrive to us at time t_0 given by:

$$\int_{t_1}^{t_0} \frac{dt}{a(t)} = \int_0^r \frac{dr}{\sqrt{1-Kr^2}}. \tag{4.21}$$

We will use the standard definitions of the fractions Ω_Λ, Ω_M and Ω_R of the critical energy density, such that the present energy densities in the vacuum, non-relativistic matter and relativistic matter are:

$$\rho_V \equiv \frac{3H_0^2\Omega_\Lambda}{8\pi G}, \tag{4.22}$$

$$\rho_M \equiv \frac{3H_0^2\Omega_M}{8\pi G}, \tag{4.23}$$

$$\rho_R \equiv \frac{3H_0^2\Omega_R}{8\pi G}, \tag{4.24}$$

and, using (4.15):

$$\Omega_\Lambda + \Omega_M + \Omega_R + \Omega_K = 1, \tag{4.25}$$

such that

$$\Omega_K \equiv -\frac{K}{a_0^2 H_0^2}. \tag{4.26}$$

Using these definitions, the energy density is:

$$\rho = \frac{3H_0^2}{8\pi G}\left[\Omega_\Lambda + \Omega_M\left(\frac{a_0}{a}\right)^3 + \Omega_R\left(\frac{a_0}{a}\right)^4\right]. \tag{4.27}$$

Furthermore, Friedmann equation (4.15) gives:

$$dt = \frac{dx}{H_0 x\sqrt{\Omega_\Lambda + \Omega_K x^{-2} + \Omega_M x^{-3} + \Omega_R x^{-4}}}, \tag{4.28}$$

where $x \equiv a/a_0 = 1/(1+z)$.

From (4.21) and (4.28) we obtain:

$$r(z) = S\left[\frac{1}{a_0 H_0}\int_{1/(1+z)}^{1} \frac{dx}{x^2\sqrt{\Omega_\Lambda + \Omega_K x^{-2} + \Omega_M x^{-3} + \Omega_R x^{-4}}}\right], \tag{4.29}$$

where

$$S[y] \equiv \begin{cases} \sin y & K = +1 \\ y & K = 0 \\ \sinh y & K = -1. \end{cases} \tag{4.30}$$

Therefore, the luminosity distance in a flat universe ($K = 0$) will be given by:

$$d_L(z) = \frac{1+z}{H_0} \int_{1/(1+z)}^{1} \frac{dx}{x^2\sqrt{\Omega_\Lambda + \Omega_M x^{-3} + \Omega_R x^{-4}}}. \tag{4.31}$$

However, adding a curvature term, Ω_K, results in:

$$\begin{aligned} d_L(z) = {} & \frac{1+z}{H_0 {\Omega_K}^{1/2}} \times \\ & \times \sinh\left[{\Omega_K}^{1/2} \int_{1/(1+z)}^{1} \frac{dx}{x^2\sqrt{\Omega_\Lambda + \Omega_K x^{-2} + \Omega_M x^{-3} + \Omega_R x^{-4}}}\right] \end{aligned} \tag{4.32}$$

On the other hand, adding the energy density Ω_w from our model to a flat universe would result in:

$$\rho = \frac{3H_0^2}{8\pi G}\left[\Omega_\Lambda + \Omega_w \left(\frac{a_0}{a}\right)^3 + \Omega_M \left(\frac{a_0}{a}\right)^3 + \Omega_R \left(\frac{a_0}{a}\right)^4\right], \tag{4.33}$$

and

$$d_L(z) = \frac{1+z}{H_0} \int_{1/(1+z)}^{1} \frac{dx}{x^2\sqrt{\Omega_\Lambda + \Omega_w x^{-2} + \Omega_M x^{-3} + \Omega_R x^{-4}}}, \tag{4.34}$$

where

$$\rho_w \equiv \frac{3H_0^2 \Omega_w}{8\pi G}. \tag{4.35}$$

Therefore we see that the effect of such a contribution to the energy density can be distinguished from the effect of curvature.

Next we will discuss the requirements on the various parameters of our model, ensuring that this form of energy density survives and makes a non-negligible contribution to the present energy density of the universe.

4.4 Spatial Size of the Toroidal Universe

There are various bounds on the spatial size of the universe when the universe is assumed to have the topology of a torus. The most stringent bound, to our knowledge, comes from the absence of ”circles in the sky” [49].

Namely, if our universe was shaped as a torus, the light from a distant source could reach us from two directions. This could be observed provided enough time has passed such that both signals arrive, or in other words provided that the universe is small enough. The farthest distance that can be observed is the surface of the last scattering, and this is where one should search for evidence of multiple imaging.

With the recent Wilkinson Microwave Anisotropy Probe (WMAP) experiment [55] we have entered the era of precision cosmology, and it is now possible to analyze the WMAP data to look for evidence of non-trivial topology of the universe.

In particular, the surface of last scattering is a 2-sphere centered around the observer. If two copies of surfaces of last scattering are separated by a distance smaller than the diameter of the surface of last scattering, the two spheres will intersect, and their intersection will be a circle. In this case, cosmic microwave background radiation coming from the surface of last scattering should have circular patterns of hot and cold spots.

Observing a circle with an angle α would correspond to a translation distance of:

$$d = 2R_{lss}\cos\alpha, \tag{4.36}$$

where R_{lss} is the distance to the last scattering surface (see Figure 4.1).

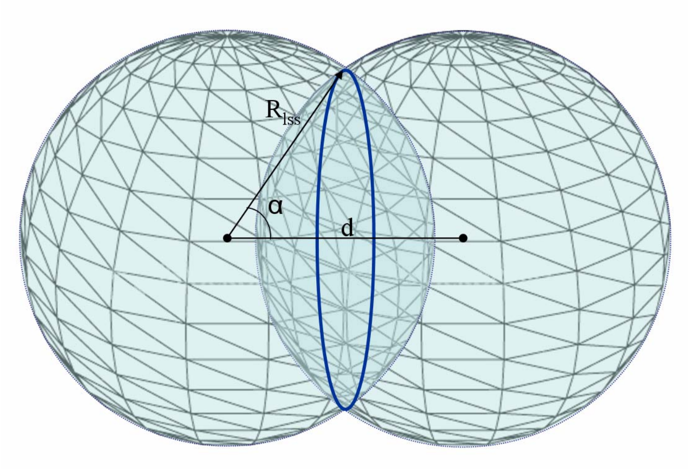

Figure 4.1: Intersection of two copies of the surface of last scattering leads to circular patterns. The size of the universe corresponds to d.

The search on the WMAP data found no statistically significant circular matches for $\alpha > 25°$ [49]. This means that the physical size of the toroidal universe should be no smaller than about six times the size of our present horizon;

$$La_0 \geq 24 \text{ Gpc} \sim 5\times 10^{61} l_P, \tag{4.37}$$

where $l_P = (\hbar G/c^3)^{1/2}$ is the Planck length.

Using the lower bound on the size of the universe, we estimate the energy density, ρ_w stored today in the "wound" scalar fields as a function of the parameter f, "the decay constant" of the θ_i.

$$\rho_w = \frac{3w^2 f^2}{2L^2 a^2} \leq \frac{3w^2 f^2}{5 \times 10^{123} {l_P}^2}, \tag{4.38}$$

which gives a contribution to the density of the universe today:

$$\frac{\rho_w}{\rho_{cr}} = \left(\frac{f \ w}{2 \times 10^{19}\mathrm{GeV}} \right)^2 . \tag{4.39}$$

A one percent contribution to the present energy density corresponds to:

$$f \sim 2 \times 10^{18}\mathrm{GeV}. \tag{4.40}$$

We can now point out an additional reason why these scalars are not expected to affect static forces between bulk matter at macroscopic distances, which is that they couple derivatively with a decay constant that is close to the Planck scale.

4.5 Remark on the Use of Classical Gravity

Even though the above-derived decay constant (4.40) is close to the Planck scale, it does not invalidate the use of classical gravity to describe the evolution of the universe.

Since for $w = -1/3$:

$$R = 8\pi G(\rho - 3p) = 16\pi G\rho, \tag{4.41}$$

using (4.11), the contribution to the Ricci scalar from this form of energy is evaluated to be:

$$R\,l_P^2 \sim 24\pi \left(\frac{l_P}{La(t)}\right)^2 \left(\frac{w\,f}{1.2\times 10^{19}\mathrm{GeV}}\right)^2 . \tag{4.42}$$

Therefore as long as the physical size of the universe exceeds $10 l_P$, the scalar curvature is safely subplanckian.

It is worth reminding the reader that we imposed earlier a restriction on parameter space by choosing the same "decay constant", f, for the θ_i to insure the isotropy of the microwave background.

4.6 Requirements Coming from Inflation

Inflation is a successful cosmological theory which assumes that early universe went through a phase of rapid accelerated expansion. This in turn helps explain the observed flatness and homogeneity of the present universe, as well as absence of relics from the hot big bang stage of the very early universe.

One of the simplest models assumes that the inflation is driven by a scalar field, inflaton. A particular feature of scalar fields is that their effective equation of state is one with a negative pressure, which is needed for inflation.

The energy density and pressure of a homogeneous scalar field ϕ are given by:

$$\rho_\phi = \frac{1}{2}\dot{\phi}^2 + V(\phi), \tag{4.43}$$

$$p_\phi = \frac{1}{2}\dot{\phi}^2 - V(\phi), \tag{4.44}$$

where $V(\phi)$ is the potential of the scalar field.

Using the continuity equation (4.13) and the Friedmann equation (4.15), and assuming a flat universe, we obtain

$$\ddot{\phi} + 3H\dot{\phi} = -\frac{dV}{d\phi} \tag{4.45}$$

and

$$H^2 = \frac{1}{3M_P^2}\Big[V(\phi) + \frac{1}{2}\dot{\phi}^2\Big], \tag{4.46}$$

where H is the Hubble constant (4.17) and M_P is the reduced Planck mass,

$$M_P \equiv (8\pi G)^{-1/2} = 2.4 \times 10^{18}\,\mathrm{GeV}. \tag{4.47}$$

In studying inflation, the so called slow-roll approximation is commonly assumed. The conditions for this approximation is that the slow-roll parameters ϵ and η, defined by [56]:

$$\epsilon(\phi) \equiv \frac{M_P^2}{2}\left(\frac{V'}{V}\right)^2, \tag{4.48}$$

$$\eta(\phi) \equiv M_P^2 \frac{V''}{V}, \tag{4.49}$$

where prime denotes derivative with respect to ϕ, satisfy:

$$\begin{aligned} \epsilon(\phi) &<< 1, \\ |\eta(\phi)| &<< 1. \end{aligned} \tag{4.50}$$

Equations (4.45) and (4.46) in the slow-roll approximation become:

$$3H\dot{\phi} \simeq -V' \tag{4.51}$$

and

$$H^2 \simeq \frac{V}{3M_P^2}. \tag{4.52}$$

There are several requirements which our model needs to fulfill coming from inflation. In particular, we need to ensure the appropriate onset of inflation, as well as the scale-invariance of the perturbation spectrum coming from inflation. This section addresses these issues.

4.6.1 Onset of Inflation

In the presence of this additional form of energy, the onset of inflation depends on the energy density stored in the scalar fields to become smaller than the energy density, Λ_I, which sets the energy density scale of inflation.

$$\rho_w(t_{bi}) << \Lambda_I, \tag{4.53}$$

where subscript bi stands for "beginning inflation".

In terms of the current energy density stored in the scalar fields:

$$\begin{aligned}\rho_w(t_0) &= \left(\frac{a(t_{ai})}{a(t_0)}\right)^2 \rho_w(t_{ai}) \\ &= \left(\frac{T(t_0)}{T_R}\right)^2 \rho_w(t_{ai}) \\ &= \left(\frac{T(t_0)}{T_R}\right)^2 \left(\frac{a(t_{bi})}{a(t_{ai})}\right)^2 \rho_w(t_{bi}) \\ &= \left(\frac{T(t_0)}{T_R}\right)^2 e^{-2N_e}\rho_w(t_{bi}),\end{aligned} \tag{4.54}$$

this constraint becomes:

$$\rho_w(t_0) << \Lambda_I e^{-2N_e}\left(\frac{T_0}{T_R}\right)^2, \tag{4.55}$$

where subscript ai stands for "after inflation", T_R is the reheating temperature, and N_e denotes the number of e-foldings during inflation.

4.6.2 Spectrum of the Fluctuations

Another important constraint comes from requiring that the fluctuations generated during inflation, in the energy density of the scalar field (in the presence of their non-trivial topological background) not overwhelm the scale invariant fluctuations produced by the inflaton.

To study the spectrum of the fluctuations of the inflaton field we assume

$$\phi(\vec{x},t) = \phi(t) + \delta\phi(\vec{x},t). \tag{4.56}$$

Using Fourier expansion

$$\delta\phi(\vec{x},t) = \sum_{\vec{k}} \delta\phi_{\vec{k}}(t) e^{i\vec{k}\vec{x}}, \tag{4.57}$$

the scalar wave equation (4.45) for a given Fourier component becomes:

$$\delta\ddot{\phi}_{\vec{k}} + 3H\delta\dot{\phi}_{\vec{k}} + \frac{k}{a^2}\delta\phi_{\vec{k}} = 0, \tag{4.58}$$

where negligible inflaton mass was assumed. Using

$$\delta\phi_{\vec{k}}(t) = w_k(t)a_{\vec{k}} + w_k^*(t){a^\dagger}_{-\vec{k}}, \tag{4.59}$$

where $w_k(t)$ satisfies:

$$\ddot{w}_k(t) + 3H\dot{w}_k(t) + \left(\frac{k}{a}\right)^2 w_k = 0, \tag{4.60}$$

we obtain the solution:

$$w_k(t) = L^{-3/2}\frac{H}{(2k^3)^{1/2}}\left(i + \frac{k}{aH}\right)\exp\left(\frac{ik}{aH}\right). \tag{4.61}$$

A few Hubble times after horizon exit $k \ll aH$, and so we can drop the second term in (4.61).

Assuming the vacuum quantum state, annihilated by $a_{\vec{k}}$, the mean square vacuum fluctuation is:

$$< |\delta\phi_{\vec{k}}|^2 >= |w_k|^2, \tag{4.62}$$

which for time $t_\star$, corresponding to a few Hubble times after horizon exit, becomes:

$$< |\delta\phi_{\vec{k}}|^2 >= \frac{H^2(t_\star)}{2L^3k^3}. \tag{4.63}$$

We define the spectrum of the fluctuations:

$$\mathcal{P}_\phi(k) = \mathcal{V}\frac{k^3}{2\pi^2}|w_k|^2, \tag{4.64}$$

such that:

$$< \phi^2(\vec{x}) >= \int_0^\infty \mathcal{P}_\phi(k)\frac{dk}{k}. \tag{4.65}$$

Therefore, using (4.63), we obtain:

$$\mathcal{P}_\phi(k, t_\star) = \left(\frac{H}{2\pi}\right)^2\Bigg|_{k=aH}, \tag{4.66}$$

where H is evaluated at the horizon exit ($k = aH$), since in the slow-roll approximation we are using, the variation of the Hubble rate is negligible over a few Hubble times.

Perturbations in the wound fields ($\delta\theta_i$) together with the perturbations of the inflaton field ($\delta\phi$) will generate a perturbation of the stress energy density. In turn, these perturbations will generate a perturbation in the metric

(Ψ). To relate this latter variable to the first two, we should construct the linear combination of these quantities that is conserved outside the horizon. It is given by [57, 58]:

$$\zeta = \frac{-ik_i \delta T^0{}_i H}{k^2(\rho + P)} - \Psi. \tag{4.67}$$

One can separately analyze the contributions to δT_i^0 from the two types of fields.

Since:

$$T^0{}_i = g^{0\alpha} \phi_{,\alpha} \phi_{,i} \,, \tag{4.68}$$

using (4.56) and (4.57), we obtain:

$$(\delta T_\phi)^0{}_i = -ik_i \frac{d\phi}{dt} \delta\phi. \tag{4.69}$$

On the other hand, for the wound fields, using:

$$\theta_i(\vec{x}, t) = \theta_i(x_i) + \delta\theta_i(\vec{x}, t) \,, \tag{4.70}$$

we obtain:

$$(\delta T_w)^0{}_i = -\frac{wf^2}{L} \frac{d\delta\theta_i}{dt}. \tag{4.71}$$

Since $|\frac{d\delta\theta_i}{dt}| = \frac{H}{\sqrt{2}} |\delta\theta_i|$ at horizon crossing, the fluctuations around the wound fields, if dominant, will generate a non scale invariant power spectrum. Both the inflaton field and the wound fields are scalars and will have the same quantum perturbations.

$$< \delta\phi(\vec{k}, t) \delta\phi(-\vec{k}, t) >= f^2 < \delta\theta_i(\vec{k}, t) \delta\theta_i(-\vec{k}, t) > . \tag{4.72}$$

Hence the condition to avoid violations of scale invariance is that:

$$\rho_w << (P_\phi + \rho_\phi) = \left(\frac{d\phi}{dt}\right)^2. \tag{4.73}$$

This condition, in turn, ensures that the contribution to Ψ from the wound fields is negligible at sub-horizon and crossing horizon scales.

4.6.3 Observational Data on Inflationary Parameters

In this section we explore the observational constraints on the various inflationary parameters discussed in the previous section. In addition, we also discuss the extent to which the $1/a^2$ contribution to the energy density could be present today.

The spectrum of the primordial curvature perturbation in the slow-roll approximation is given by [56]:

$$\Delta_R^2(k) = \left[\left(\frac{H}{\dot{\phi}}\right)^2 \mathcal{P}_\phi(k)\right]_{t=t_*}. \tag{4.74}$$

Using (4.66) we obtain:

$$\Delta_R^2(k) = \left[\left(\frac{H}{\dot{\phi}}\right)\left(\frac{H}{2\pi}\right)\right]^2_{k=aH}. \tag{4.75}$$

Furthermore, from (4.48), (4.51), (4.52):

$$\epsilon = \frac{3}{2}\frac{\dot{\phi}}{V}, \tag{4.76}$$

leading to

$$\Delta_R^2(k_0) = \frac{V/M_P^4}{24\pi^2\epsilon}. \tag{4.77}$$

The relative amplitude of the tensor to scalar modes r is defined by:

$$r \equiv \frac{\Delta_h^2(k_0)}{\Delta_R^2(k_0)}, \tag{4.78}$$

where the gravitational-wave spectrum is given by:

$$\Delta_h^2 = \frac{8}{M_P^2}\left(\frac{H}{2\pi}\right)^2. \tag{4.79}$$

Using (4.76) this gives:

$$r = 16\epsilon. \tag{4.80}$$

Recent WMAP data [59] yields values

$$r(k_0 = 0.002\,\mathrm{Mpc}^{-1}) < 0.90, \tag{4.81}$$

$$A(k_0 = 0.002\,\mathrm{Mpc}^{-1}) = 0.75^{+0.08}_{-0.09}, \tag{4.82}$$

where $A(k_0)$ and $\Delta_R^2(k_0)$ are related through

$$\Delta_R^2(k_0) \simeq 2.95 \times 10^{-9} A(k_0). \tag{4.83}$$

From (4.77) and (4.80) we see that the WMAP data corresponds to

$$\dot{\phi} \simeq 2 \times 10^{-34} \frac{V}{\mathrm{GeV}^2}, \tag{4.84}$$

$$V < (3.1 \times 10^{16}\,\mathrm{GeV})^4. \tag{4.85}$$

We have previously obtained the requirement (4.73):

$$\rho_w < \dot{\phi}^2. \tag{4.86}$$

Assuming that the modes of the size of present horizon left the horizon during inflation N_e e-foldings before the end of the inflation, which in our scenario is the beginning of inflation, and also assuming maximally efficient reheating ($T_R^4 = V$), using (4.38), (4.54) and (4.86) we obtain:

$$\rho_w(t_0) = \frac{3}{2}\left(\frac{wf}{La_0}\right)^2 < \dot{\phi}^2 e^{-2N_e}\frac{T_0^2}{\sqrt{V}}, \tag{4.87}$$

which, taking $\rho_w < \frac{1}{10}\dot{\phi}^2$ and using (4.84), leads to:

$$f < 1.2 \times 10^{-47} e^{-N_e} V^{3/4} La_0/\text{GeV}. \tag{4.88}$$

In particular, taking $La_0 \sim 24\,\text{Gpc}$, $V \sim (3 \times 10^{16}\,\text{GeV})^4$ and $N_e = 60$ we obtain the limit:

$$f < 10^{19}\,\text{GeV}. \tag{4.89}$$

This constraint turns out to be more stringent than the one obtained from considerations regarding the onset of inflation. Namely, comparing the two conditions, and using the value of V as above, we see that the condition (4.55) is weaker than the condition (4.87) by a factor of $\sqrt{V}/\dot{\phi} \sim 10$. Therefore, (4.89) represents the overall bound coming from inflation considerations.

4.7 Other Constraints

In addition to insuring that our model is consistent with inflation and its predictions, there are several other constraints on the parameters of our model coming from cosmological observations. Here we will address a few.

4.7.1 High-Redshift Supernova Measurements

There are additional constraints from the observational data which can potentially limit the contribution of $1/a^2$ term to the present energy density. One of the strongest evidences for the acceleration of our present universe comes from the studies of Type Ia supernovae. In accelerating universe, distant supernovae (redshifts $z \approx 0.5$) will appear to be dimmer than what one would expect in a universe expanding at a constant rate. Such observations give us limits on the distribution of energy density in the universe, and lead to predictions of the present amount of dark energy.

In particular, recent high-redshift supernova measurements [60] seem to allow a flat universe with e.g. $\Omega_M \simeq 0.27$ and $\Omega_\Lambda \simeq 0.53$, within the 95% confidence level, which in our model would correspond to $\Omega_w \simeq 0.20$ (Ω_w being the contribution of $1/a^2$ term to the present energy density).

4.7.2 Age of the Universe

A considerable Ω_w would also have an effect on the age of the universe, which might provide an additional constraint on our model.

From (4.28), assuming a flat universe ($\Omega_K = 0$) and a fraction of energy density Ω_w in wound fields given by (4.35), we obtain the current age of the universe:

$$H_0 t_0 = \int_0^\infty \frac{dz}{1+z}\Big[\Omega_\Lambda + \Omega_w(1+z)^2 + \Omega_M(1+z)^3 + \Omega_R(1+z)^4\Big]^{-1/2}. \quad (4.90)$$

In particular, for a flat universe with:

$$\begin{aligned} \Omega_M &= 0.27 \pm 0.04, \\ \Omega_w &= 0.2, \\ \Omega_R &= 10^{-4}, \\ \Omega_\Lambda &= 1 - \Omega_M - \Omega_R - \Omega_w, \\ H_0 &= 72 \pm 3 \pm 7\,\mathrm{km\,s^{-1}\,Mpc^{-1}}, \end{aligned} \tag{4.91}$$

one obtains the age of the universe to be:

$$t_0 = 13 \pm 2\,\mathrm{Gyr}, \tag{4.92}$$

where the value for Ω_M is from [59], and the value for H_0 from the HST Key Project [61].

This is consistent with the present observational data coming from cosmic microwave background radiation considerations [55]; age of metal-poor stars obtained from the observations of stellar abundances of stable elements [62]; as well as the globular clusters age estimates [63, 64].

Therefore even a 20% contribution to the present energy density in this form would not be excluded on the basis of considerations of the current age of the universe.

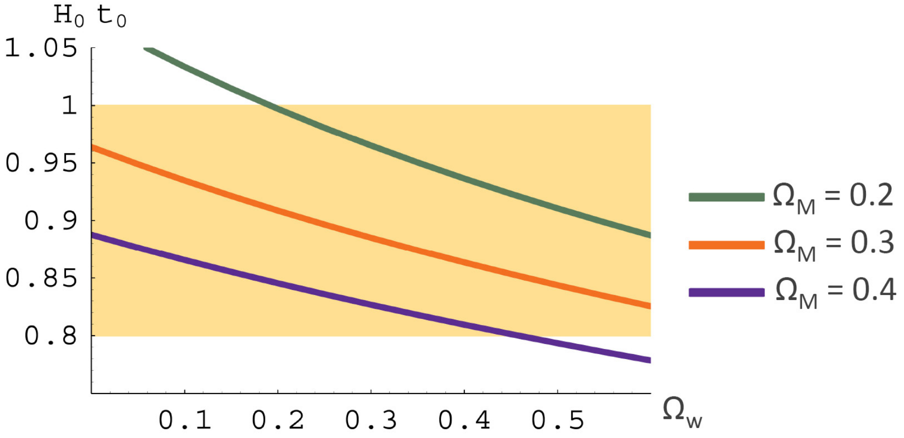

Figure 4.2: The effect of $\Omega_w = 1 - \Omega_M - \Omega_\Lambda$ on the age of the universe. The light yellow region corresponds to the globular cluster age $t_0 = 12.7 \pm 0.7\,\mathrm{Gyr}$ [63]. Plot uses the HST Key Project [61] value of $H_0 = 72 \pm 8\,\mathrm{km\,s^{-1}\,Mpc^{-1}}$.

4.8 Conclusions

The experimental data seem to leave open the possibility of a contribution to the present energy that redshifts like $1/a^2$. In this chapter we presented a rather constrained setup that cannot yet be excluded experimentally and does yield such a contribution to today's energy density.

There are, in addition, other known sources for a component of the energy density that behaves like $1/a^2$. Among these are models of texture [65], which is a type of a cosmological topological defect. However, these topological defects decay, leading to generation of cosmic structure [66], with a distribution excluded by the observational data of spatial clustering of clusters of galaxies [67].

Another source that would lead to $1/a^2$ contribution to the present energy density are cosmic strings [68–70]. It is unclear, however, whether these sources would contribute in such manner today [71].

Our hope is that the experiments will put firmer bounds on the existence of a $1/a^2$ contribution to the present energy density, irrespective of what sources such contribution.

Chapter 5

Concluding Remarks

The interface of cosmology with string theory is an extremely exciting and important area of current research. The problems arising at this interface are numerous, and this thesis is inspired by and touches upon just a few of them.

First, we investigated evolution of certain classically unstable de Sitter compactifications. This research was motivated by the work of Bousso, DeWolfe and Myers [11] who studied $dS_p \times S^q$ - type solutions with flux arising in gravity with a positive cosmological constant. Among the stable solutions of this form they found solutions with unbounded entropy, thus leading to the conclusion that a positive cosmological constant alone is not sufficient to characterize classes of spacetimes with finite-dimensional Hilbert spaces. In addition, they found some unstable solutions of $dS_p \times S^q$ form, and posed the question of the fate of these solutions. This was the question we addressed in Chapter 2 of this thesis. In order to study the time evolution of named solutions, we looked at a broader set of solutions that in general do not correspond to product spacetimes, but rather have a time-dependent radius of the extra dimensions. This construction allowed us to numerically follow the evolution, and led us to the discovery of additional stable solutions that the original, unstable solutions tend toward for a certain range of fluxes. We found that in this process de Sitter space ends up with a smaller final effective cosmological constant. For other values of flux, we find that the internal sphere decompactifies, in which case it either expands at the same rate as the de Sitter dimensions, or it might also happen that the de Sitter space contracts in the process.

The spacetimes we investigated have additional unstable modes not studied in our current work. This would be the natural extension of this analysis. In addition, it would be interesting to further these studies by looking into more realistic compactification models, from the viewpoint of string theory, as well as addressing non-classical effects of thermal fluctuations and tunneling.

Next, we discussed the problem of evolution of vacuum bubbles in inhomogeneous backgrounds. It is expected that the process of inflation will significantly smooth out spatial inhomogeneities. However, the initial conditions for inflation are often taken in the already homogeneous and isotropic FRW form, even though it is assumed that initial homogeneity is not necessary for the onset of inflation. We feel that a better understanding of constraints on the homogeneity of space at the onset of inflation is needed. Moreover, this is particularly important in the context of the landscape of vacua where generic backgrounds are more likely to be inhomogeneous than not. In Chapter 3 we saw the effects of certain inhomogeneities on the propagation of vacuum bubbles, which were obtained through numerical simulations. In particular, we learned that from the point of view of the outside coordinates, matter and inhomogeneities introduced through the background curvature can have a significant effect on the bubble evolution. However, from the point of view of the coordinates on the bubble, such inhomogeneities have only negligible effects on the bubble propagation, and the bubble in most cases inflates, as long as the outside space itself does not go through a crunch.

To continue these studies, more examples of the inhomogeneities should be looked at, with variable initial conditions. In our current analysis we assumed the inside of the bubble to be empty and introduced inhomogeneities through background curvature only. In addition we imposed a particular equation of state on the surface of the bubble. This led to a rather specific and somewhat constrained investigation. A better understanding of the nature of the tunneling process through which these bubbles are created with certain restrictions and initial conditions would allow further progress of our studies.

Finally, we looked at a model which can account for a significant contribution to the present energy density of the universe. The model is based on the assumption of toroidal topology of the universe, and it introduces scalar fields that are wound around the torus cycles. This results in a component of the energy density which redshifts as $1/a^2$.

We investigated various observational constraints the model needs to satisfy; limits coming from the size and topology of the universe, effects of the model on the age of the universe, onset of inflation, as well as effects on the spectrum of the fluctuations observed in the CMBR. This analysis led to the conclusion that this model could source a contribution of roughly 1% to the present energy density of the universe. We expect that the future observational data will provide more stringent constraints not only on this model, but on any model that produces contributions of the $1/a^2$ type.

Future studies of the interplay of cosmology with physics beyond the Standard Model will undoubtedly have profound effects on our understanding of the shape and nature of our universe.

Appendices

Appendix A

This is an example of the Wolfram Mathematica file used to generate time evolution plots in Chapter 2. This file leads to the Figure 2.8.

<< Graphics`MultipleListPlot`

$\beta = 0.15;$

$d = 1/100;$

$t[\mathrm{n\_}] = n * d;$

$\mathrm{nmax} = 2500;$

$F[\mathrm{x\_}, \mathrm{y\_}] := \frac{x}{2} + \frac{3}{2}\frac{\beta}{x^3} - \frac{1}{x} + 2\frac{y^2}{x} - \frac{3}{2}y\sqrt{\frac{8}{3}\frac{y^2}{x^2} - \frac{4}{3}\left(\frac{1}{x^2} - 1 - \frac{\beta}{x^4}\right)}$

$\mathrm{For}[k = 1, k \leq 13,$

$\mathrm{Clear}[x, y];$

$\mathrm{Switch}[k, 1, \{x[0] = 2, y[0] = -2\}, 2, \{x[0] = 1.5, y[0] = -2\},$

$3, \{x[0] = 1, y[0] = -2\}, 4, \{x[0] = .45, y[0] = -2\},$

$5, \{x[0] = .25, y[0] = -2.5\}, 6, \{x[0] = .35, y[0] = -2\},$

$7, \{x[0] = .3, y[0] = -2\}, 8, \{x[0] = .63, y[0] = -2\},$

$9, \{x[0] = .81, y[0] = -2\}, 10, \{x[0] = 1.25, y[0] = -2\},$

$11, \{x[0] = 1.75, y[0] = -2\}, 12, \{x[0] = 2.17, y[0] = -2\},$

$13, \{x[0] = 1.9, y[0] = -2\}];$

$\mathrm{For}[n = 1, n \leq \mathrm{nmax},$

$x[n] = x[n-1] + y[n-1] * d;$

$y[n] = y[n-1] + F[x[n], y[n-1]] * d;$

$n{+}{+}];$

$z[k] = \mathrm{Table}[\{x[n], y[n]\}, \{n, \mathrm{nmax}\}];$

$k{+}{+}]$

$\mathrm{Clear}[x, y]$

$$\mathrm{Solve}\left[-\frac{y}{x} + \frac{1}{2}\sqrt{\frac{8}{3}\frac{y^2}{x^2} - \frac{4}{3}\left(\frac{1}{x^2} - 1 - \frac{.15}{x^4}\right)} == 0, y\right]$$

$$\left\{\left\{y \to -1.52349 \times 10^{-8} \sqrt{-4.30844 \times 10^{15} + \frac{6.46266\times10^{14}}{x^2} + 4.30844 \times 10^{15} x^2}\right\},\right.$$
$$\left.\left\{y \to 1.52349 \times 10^{-8} \sqrt{-4.30844 \times 10^{15} + \frac{6.46266\times10^{14}}{x^2} + 4.30844 \times 10^{15} x^2}\right\}\right\}$$

$$\mathrm{w1[x\_]:=1.5234912189342865\grave{}{*}\hat{}{-8}}$$
$$\sqrt{}\left(-4.30844039633288\grave{}{*}\hat{}15 + \frac{6.46266059449932\grave{}{*}\hat{}14}{x^2} + 4.30844039633288\grave{}{*}\hat{}15 x^2\right)$$

$\mathrm{Clear}[x, y]$

$$\mathrm{Solve}\left[\frac{8}{3}\frac{y^2}{x^2} - \frac{4}{3}\left(\frac{1}{x^2} - 1 - \frac{.15}{x^4}\right) == 0, y\right]$$

$$\left\{\left\{y \to -0.612372\sqrt{-1.33333 - \frac{0.2}{x^4} + \frac{1.33333}{x^2}}x\right\},\right.$$
$$\left.\left\{y \to 0.612372\sqrt{-1.33333 - \frac{0.2}{x^4} + \frac{1.33333}{x^2}}x\right\}\right\}$$

$$\mathrm{w2[x\_]:=0.6123724356957945\grave{}}$$
$$\sqrt{}\left(-1.3333333333333333\grave{} - \frac{0.19999999999999998\grave{}}{x^4} + \frac{1.3333333333333333\grave{}}{x^2}\right) x$$

```
x[n_]:=.001 + 0.001 ∗ n;
b1 = Table[{x[n], w1[x[n]]}, {n, 1000}];
b2 = Table[{x[n], w2[x[n]]}, {n, 1000}];
b3 = Table[{x[n], −w2[x[n]]}, {n, 1000}];

MultipleListPlot[z[1], z[2], z[3], z[4], z[5], z[6],
z[7], z[8], z[9], z[10], z[11], z[12], z[13], b1, b2,
b3, PlotJoined → True, SymbolShape → None,
PlotStyle → {Hue[0.7], Hue[0.7], Hue[0.7], Hue[0.7],
Hue[0.7], Hue[0.7], Hue[0.7], Hue[0.7], Hue[0.7],
Hue[0.7], Hue[0.7], Hue[0.7], Hue[0.7], Hue[0, 0, 0],
Hue[0, 0, 0], Hue[0, 0, 0]},
PlotRange → {{0, 2}, {−.7, .7}}, AxesLabel->{R√Λ, Ṙ},
AspectRatio → .45]
```

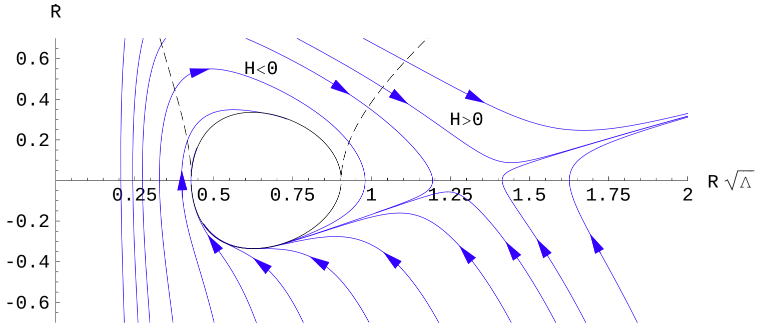

Appendix B

This is an example of the Wolfram Mathematica file used to generate bubble evolution plots in Chapter 3. This file leads to the Figures 3.7 and 3.8.

```
<< Graphics`Graphics3D`

<< Graphics`MultipleListPlot`

Clear[F, λ, nmax, dt, s, x, R, b, n, m, a, ap, o, B, kp, x, v, τ, z1,
ninit, t, w, sinit, adot, dif, B1, pot, phase, sf, p, l]
λ = 3 * $10^{-5}$;
R = 500;
F = $10^{-4}$;
nmax = 10000;
ninit = 1;
dt = .1;
p = 1;
b[a_]:=$\sqrt{\frac{F}{a} + \frac{\lambda * a^2}{3} - \frac{1}{R^2}}$;
s[ninit] = .001;
τ[ninit] = 0;
a[0] = 1;
```

$\mathrm{For}[k = 1, k \leq \mathrm{ninit}, k{+}{+},$

$a[k] = a[k-1] + b[a[k-1]] * \mathrm{dt};$

$\mathrm{For}[l = p, l \leq p + 3,$

$\mathrm{Switch}[l, p, w = 1/3, p+1, w = 0, p+2, w = -1/3, p+3, w = -1];$

$\mathrm{For}[n = \mathrm{ninit}, n \leq \mathrm{nmax},$

$a[n] = a[n-1] + b[a[n-1]] * \mathrm{dt};$

$o[n] = \frac{\lambda}{3} + \frac{F}{a[n]^3};$

$\mathrm{adot}[n] = b[a[n]];$

$B[n] = \frac{4 * o[n] + s[n]^2}{4 * s[n]};$

$x[\mathrm{ninit}] = 10;$

$\mathrm{kp}[n] = 1 \Big/ \left(x[n] * a[n]^2 * \left(B[n]^2 - \frac{1}{a[n]^2 R^2}\right)\right)$
$\left(-\frac{\mathrm{adot}[n]}{a[n]}\left(1 - \frac{x[n]^2}{R^2}\right) + \right.$
$\left.\sqrt{\left(((B[n] * a[n] * x[n])^2 - 1)\,(B[n]^2 - o[n])\left(1 - \frac{x[n]^2}{R^2}\right)\right)}\right);$

$x[n+1] = x[n] + \mathrm{kp}[n] * \mathrm{dt};$

$s[n+1] =$

$s[n] -$

$\left(2 * s[n] * (1 + w) * \left(\frac{\mathrm{adot}[n]}{a[n]} + \frac{\mathrm{kp}[n]}{x[n]}\right) - \right.$

$\left.\frac{3 * F}{a[n]^2} * \mathrm{kp}[n] * \frac{1}{\sqrt{1 - \frac{x[n]^2}{R^2} - \mathrm{kp}[n]^2 * a[n]^2}}\right) * \mathrm{dt};$

$v[n] = \sqrt{1 - \frac{a[n]^2}{1 - \frac{x[n]^2}{R^2}} * \mathrm{kp}[n]^2};$

$\tau[n+1] = \tau[n] + v[n] * \mathrm{dt};$

$t[n] = n * \mathrm{dt};$

$n{+}{+}];$

```
wx[l] = Table[{t[n], x[n]}, {n, ninit, nmax}];
Ax[l] = Table[{t[n], 1/(B[n] * a[n])}, {n, ninit, nmax}];
bub[l] = Table[{τ[n], x[n] * a[n]}, {n, ninit, nmax}];
si[l] = Table[{t[n], s[n]}, {n, ninit, nmax}];
l++]
```

```
xfullfixed500:=MultipleListPlot[wx[1], wx[2], wx[3], wx[4],
wx[5], wx[6], wx[7], wx[8], wx[9], wx[10], wx[11], wx[12],
PlotJoined → True, SymbolShape → None,
PlotStyle → {Hue[0], Hue[0.15], Hue[0.3], Hue[0.6], Hue[0],
Hue[0.15], Hue[0.3], Hue[0.6], Hue[0], Hue[0.15], Hue[0.3], Hue[0.6]}]
```

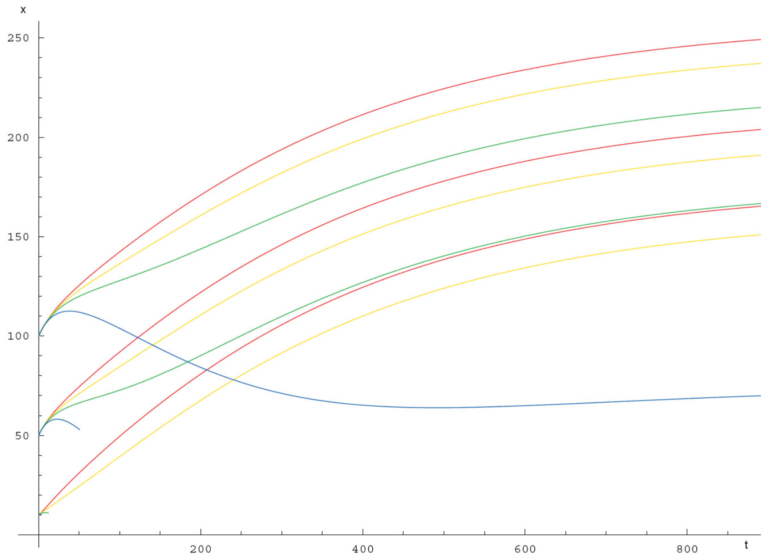

```
rhofullfixed500:=MultipleListPlot[bub[1], bub[2], bub[3], bub[4],
bub[5], bub[6], bub[7], bub[8], bub[9], bub[10], bub[11],
bub[12], PlotJoined → True, SymbolShape → None,
PlotStyle → {Hue[0], Hue[0.15], Hue[0.3], Hue[0.6], Hue[0],
Hue[0.15], Hue[0.3], Hue[0.6], Hue[0], Hue[0.15], Hue[0.3], Hue[0.6]}]
```

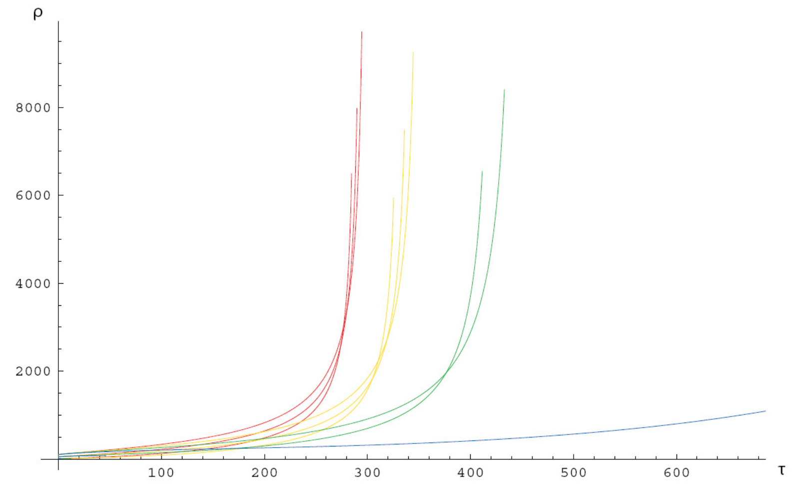

Bibliography

[1] D. N. Spergel *et al.* [WMAP Collaboration], "First Year Wilkinson Microwave Anisotropy Probe (WMAP) Observations: Determination of Cosmological Parameters," Astrophys. J. Suppl. **148**, 175 (2003) [arXiv:astro-ph/0302209].

[2] D. N. Spergel *et al.* [WMAP Collaboration], "Wilkinson Microwave Anisotropy Probe (WMAP) three year results: Implications for cosmology," Astrophys. J. Suppl. **170**, 377 (2007) [arXiv:astro-ph/0603449].

[3] A. A. Penzias and R. W. Wilson, "A Measurement of excess antenna temperature at 4080-Mc/s," Astrophys. J. **142**, 419 (1965).

[4] A. H. Guth, "The Inflationary Universe: A Possible Solution To The Horizon And Flatness Problems," Phys. Rev. D **23**, 347 (1981).

[5] S. Kachru, R. Kallosh, A. Linde, J. M. Maldacena, L. P. McAllister and S. P. Trivedi, "Towards inflation in string theory," JCAP **0310**, 013 (2003) [arXiv:hep-th/0308055].

[6] G. R. Dvali and S. H. H. Tye, "Brane inflation," Phys. Lett. B **450**, 72 (1999) [arXiv:hep-ph/9812483].

[7] A. G. Riess *et al.* [Supernova Search Team Collaboration], "Observational Evidence from Supernovae for an Accelerating Universe and a Cosmological Constant," Astron. J. **116**, 1009 (1998) [arXiv:astro-ph/9805201].

[8] W. Fischler, A. Kashani-Poor, R. McNees and S. Paban, "The acceleration of the universe, a challenge for string theory," JHEP **0107**, 003 (2001) [arXiv:hep-th/0104181].

[9] L. Susskind, "The anthropic landscape of string theory," arXiv:hep-th/0302219.

[10] L. P. McAllister and E. Silverstein, "String Cosmology: A Review," arXiv:0710.2951 [hep-th].

[11] R. Bousso, O. DeWolfe and R. C. Myers, "Unbounded entropy in spacetimes with positive cosmological constant," Found. Phys. **33**, 297 (2003) [arXiv:hep-th/0205080].

[12] C. Krishnan, S. Paban and M. Zanic, "Evolution of gravitationally unstable de Sitter compactifications," JHEP **0505**, 045 (2005) [arXiv:hep-th/0503025].

[13] W. Fischler, C. Krishnan, S. Paban and M. Zanic, "Vacuum Bubble in an Inhomogeneous Cosmology: A Toy Model," arXiv:0711.3417 [hep-th].

[14] W. Fischler, S. Paban and M. Zanic, "The Energy Density of Wound Fields in a Toroidal Universe," JHEP **0410**, 041 (2004) [arXiv:astro-ph/0407349].

[15] P. G. O. Freund and M. A. Rubin, "Dynamics Of Dimensional Reduction," Phys. Lett. B **97**, 233 (1980).

[16] G. W. Gibbons and S. W. Hawking, "Cosmological Event Horizons, Thermodynamics, And Particle Creation," Phys. Rev. D **15**, 2738 (1977).

[17] W. Fischler: Taking de Sitter seriously. Talk given at Role of Scaling Laws in Physics and Biology (Celebrating the 60th Birthday of Geoffrey West), Santa Fe, Dec. 2000.

[18] T. Banks, "Cosmological breaking of supersymmetry or little Lambda goes back to the future. II," arXiv:hep-th/0007146.

[19] R. Bousso, "Positive vacuum energy and the N-bound," JHEP **0011**, 038 (2000) [arXiv:hep-th/0010252].

[20] O. DeWolfe, D. Z. Freedman, S. S. Gubser, G. T. Horowitz and I. Mitra, "Stability of AdS(p) x M(q) compactifications without supersymmetry," Phys. Rev. D **65**, 064033 (2002) [arXiv:hep-th/0105047].

[21] C. R. Contaldi, L. Kofman and M. Peloso, "Gravitational instability of de Sitter compactifications," JCAP **0408**, 007 (2004) [arXiv:hep-th/0403270].

[22] S. Kachru, R. Kallosh, A. Linde and S. P. Trivedi, "De Sitter vacua in string theory," Phys. Rev. D **68**, 046005 (2003) [arXiv:hep-th/0301240].

[23] A. Saltman and E. Silverstein, "A new handle on de Sitter compactifications," arXiv:hep-th/0411271.

[24] S. B. Giddings and R. C. Myers, "Spontaneous decompactification," Phys. Rev. D **70**, 046005 (2004) [arXiv:hep-th/0404220].

[25] Y. Okada, "Inflation In Kaluza-Klein Cosmology," Phys. Lett. B **150**, 103 (1985).

[26] E. W. Kolb, "Cosmology And Extra Dimensions," FERMILAB-PUB-86-138-A

[27] W. Israel, "Singular Hypersurfaces And Thin Shells In General Relativity," Nuovo Cim. B **44S10**, 1 (1966) [Erratum-ibid. B **48**, 463 (1967 NUCIA,B44,1.1966)].

[28] V. A. Berezin, V. A. Kuzmin and I. I. Tkachev, "Dynamics Of Bubbles In General Relativity," Phys. Rev. D **36**, 2919 (1987).

[29] K. Lake, "Equation Of Motion For Bubble Boundaries," Phys. Rev. D **29** (1984) 1861.

[30] S. Khakshournia and R. Mansouri, "Formation of cosmological mass condensation within a FRW universe: exact general relativistic solutions," Phys. Rev. D **65**, 027302 (2002) arXiv:gr-qc/0307023].

[31] A. Vilenkin, "The Birth Of Inflationary Universes," Phys. Rev. D **27**, 2848 (1983).

[32] S. W. Hawking and T. Hertog, "Populating the landscape: A top down approach," Phys. Rev. D **73**, 123527 (2006) [arXiv:hep-th/0602091].

[33] S. W. Hawking and I. G. Moss, "Supercooled Phase Transitions In The Very Early Universe," Phys. Lett. B **110**, 35 (1982).

[34] R. W. Wald, "Asymptotic Behavior Of Homogeneous Cosmological Models In The Presence Of A Positive Cosmological Constant," Phys. Rev. D **28**, 2118 (1983).

[35] D. S. Goldwirth and T. Piran, "Initial conditions for inflation," Phys. Rept. **214**, 223 (1992).

[36] D. S. Goldwirth and T. Piran, "Inhomogeneity And The Onset Of Inflation," Phys. Rev. Lett. **64**, 2852 (1990).

[37] D. S. Goldwirth and T. Piran, "Spherical Inhomogeneous Cosmologies And Inflation. 1. Numerical Methods," Phys. Rev. D **40**, 3263 (1989).

[38] H. Kurki-Suonio, P. Laguna and R. A. Matzner, "Inhomogeneous inflation: Numerical evolution," Phys. Rev. D **48**, 3611 (1993) [arXiv:astro-ph/9306009].

[39] A. Berera and C. Gordon, "Inflationary initial conditions consistent with causality," Phys. Rev. D **63**, 063505 (2001) [arXiv:hep-ph/0010280].

[40] N. Deruelle and D. S. Goldwirth, "Conditions for inflation in an initially inhomogeneous universe," Phys. Rev. D **51**, 1563 (1995) [arXiv:gr-qc/9409056].

[41] O. Iguchi, H. Ishihara and J. Soda, "Inhomogeneity of spatial curvature for inflation," Phys. Rev. D **55**, 3337 (1997) [arXiv:gr-qc/9606012].

[42] O. Iguchi and H. Ishihara, "Onset of inflation in inhomogeneous cosmology," Phys. Rev. D **56**, 3216 (1997) [arXiv:gr-qc/9611047].

[43] G. Lemaitre, "The expanding universe," Gen. Rel. Grav. **29**, 641 (1997) [Annales Soc. Sci. Brux. Ser. I Sci. Math. Astron. Phys. A **53**, 51 (1933)].

[44] R. C. Tolman, "Effect of imhomogeneity on cosmological models," Proc. Nat. Acad. Sci. **20**, 169 (1934).

[45] H. Bondi, "Spherically symmetrical models in general relativity," Mon. Not. Roy. Astron. Soc. **107**, 410 (1947).

[46] L. F. Abbott, D. Harari and Q. H. Park, "Vacuum Decay in Curved Backgrounds," Class. Quant. Grav. **4**, L201 (1987).

[47] P. J. E. Peebles, "The Gravitational Instability of the Universe," Astrophys. J. **147**, 859 (1967).

[48] S. R. Coleman and F. De Luccia, "Gravitational Effects On And Of Vacuum Decay," Phys. Rev. D **21**, 3305 (1980).

[49] N. J. Cornish, D. N. Spergel, G. D. Starkman and E. Komatsu, "Constraining the Topology of the Universe," Phys. Rev. Lett. **92**, 201302 (2004) [arXiv:astro-ph/0310233].

[50] A. de Oliveira-Costa, G. F. Smoot and A. A. Starobinsky, "Constraining topology with the CMB," Astrophys. J. **468**, 457 (1996) [arXiv:astro-ph/9705125].

[51] J. P. Uzan, R. Lehoucq and J. P. Luminet, "New developments in the search for the topology of the universe," arXiv:gr-qc/0005128.

[52] J. Levin, "Topology and the cosmic microwave background," Phys. Rept. **365**, 251 (2002) [arXiv:gr-qc/0108043].

[53] R. R. Caldwell and M. Kamionkowski, "Expansion, Geometry, and Gravity," [arXiv:astro-ph/0403003].

[54] S. Weinberg, Lecture Notes from the Cosmology course, taught at the University of Texas at Austin, Fall 2004.

[55] C. L. Bennett *et al.*, "First Year Wilkinson Microwave Anisotropy Probe (WMAP) Observations: Preliminary Maps and Basic Results," Astrophys. J. Suppl. **148**, 1 (2003) [arXiv:astro-ph/0302207].

[56] A. R. Liddle and D. H. Lyth, "Cosmological Inflation and Large-Scale Structure", Cambridge University Press, 2000.

[57] J. M. Bardeen, "Gauge Invariant Cosmological Perturbations," Phys. Rev. D **22**, 1882 (1980).

[58] S. Dodelson, "Modern Cosmology", Elsevier Science, 2003.

[59] H. V. Peiris *et al.*, "First year Wilkinson Microwave Anisotropy Probe (WMAP) observations: Implications for inflation," Astrophys. J. Suppl. **148**, 213 (2003) [arXiv:astro-ph/0302225].

[60] A. G. Riess *et al.* [Supernova Search Team Collaboration], "Type Ia Supernova Discoveries at $z > 1$ From the Hubble Space Telescope: Evidence for Past Deceleration and Constraints on Dark Energy Evolution," [arXiv:astro-ph/0402512]. Astrophys. J. **607**, 665 (2004)

[61] W. L. Freedman *et al.*, "Final Results from the Hubble Space Telescope Key Project to Measure the Hubble Constant," Astrophys. J. **553**, 47 (2001) [arXiv:astro-ph/0012376].

[62] J. J. Cowan *et al.*, "R-Process Abundances and Chronometers in Metal-Poor Stars," Astrophys. J. **521**, 194 (1999) [arXiv:astro-ph/9808272].

[63] B. M. S. Hansen *et al.*, "The White Dwarf Cooling Sequence of the Globular Cluster Messier 4," Astrophys. J. **574**, L155 (2002) [arXiv:astro-ph/0205087].

[64] I. Neill Reid, "Younger and Brighter - New Distances to Globular Clusters Based on HIPPARCOS Parallax Measurements of Local Subdwarfs" Astronomical J. **114**, 161 (1997)

[65] R. L. Davis, "Texture: A cosmological topological defect" Phys. Rev. **D35**, 3705 (1987).

[66] N. Turok, “Global Texture as the Origin of Cosmic Structure,” Phys. Rev. Lett. **63**, 2625 (1989).

[67] R. Cen, “A critical test of topological defect models: Spatial clustering of clusters of galaxies,” Astrophys. J. **491**, 1 (1997) [arXiv:astro-ph/9707240].

[68] D. Spergel and U. L. Pen, “Cosmology in a string-dominated universe,” Astrophys. J. **491**, L67 (1997) [arXiv:astro-ph/9611198].

[69] E. J. Copeland, R. C. Myers and J. Polchinski, “Cosmic F- and D-strings,” JHEP **0406**, 013 (2004) [arXiv:hep-th/0312067].

[70] M. Kamionkowski and N. Toumbas, “A Low-Density Closed Universe,” Phys. Rev. Lett. **77**, 587 (1996) [arXiv:astro-ph/9601147].

[71] P. McGraw, “Evolution of a non-Abelian cosmic string network,” Phys. Rev. D **57**, 3317 (1998) [arXiv:astro-ph/9706182].

Vita

Marija Žanić was born in Vinkovci, Croatia on May 1, 1972, the daughter of Dinka Maretić - Žanić and Gvozdan Žanić. She received an advanced graduate-level degree in Physics (*Diplomirani Inžinjer Fizike*) from the University of Zagreb, Croatia in 1998 with a thesis titled *"Axions and Their Role in Astrophysics and Cosmology"*. After working as a Technology Analyst with Technology Strategic Planning, Inc. in 1999-2000, she enrolled in the Graduate Program in Physics at the University of Texas at Austin in 2001. Over the course of her graduate studies she participated in the competitive summer programs *Prospects in Theoretical Physics* at the Institute for Advanced Study in Princeton, NJ in the summers of 2002-2004, as well as *Frontiers of Mathematical Physics* at the University of British Columbia, Vancouver in summer 2004. Upon graduation she will join the Max Planck Institute of Molecular Cell Biology and Genetics in Dresden, Germany as a postdoctoral research fellow.

Permanent address: 7122 Wood Hollow Dr Apt 46
Austin, Texas 78731

This dissertation was typeset with LaTeX[†] by the author.

[†] LaTeX is a document preparation system developed by Leslie Lamport as a special version of Donald Knuth's TeX Program.